



**HAL**  
open science

## Seismic signature of a river flooding in La Réunion Island during the tropical cyclone Dumazile (March 2018)

Alicia Gonzalez, Fabrice R. Fontaine, Guilhem Barruol, Alain Recking, Arnaud Burtin, Laurent Michon, Jean-Lambert Join, Eric Delcher, Florent Gimbert

### ► To cite this version:

Alicia Gonzalez, Fabrice R. Fontaine, Guilhem Barruol, Alain Recking, Arnaud Burtin, et al.. Seismic signature of a river flooding in La Réunion Island during the tropical cyclone Dumazile (March 2018). *Journal of Applied Geophysics*, 2023, 215, pp.105127. 10.1016/j.jappgeo.2023.105127. insu-04164897

**HAL Id: insu-04164897**

**<https://insu.hal.science/insu-04164897v1>**

Submitted on 18 Jul 2023

**HAL** is a multi-disciplinary open access archive for the deposit and dissemination of scientific research documents, whether they are published or not. The documents may come from teaching and research institutions in France or abroad, or from public or private research centers.

L'archive ouverte pluridisciplinaire **HAL**, est destinée au dépôt et à la diffusion de documents scientifiques de niveau recherche, publiés ou non, émanant des établissements d'enseignement et de recherche français ou étrangers, des laboratoires publics ou privés.



Distributed under a Creative Commons Attribution - NonCommercial 4.0 International License



## Seismic signature of a river flooding in La Réunion Island during the tropical cyclone Dumazile (March 2018)

A. Gonzalez<sup>a,b</sup>, F.R. Fontaine<sup>a,b,c,\*</sup>, G. Barruol<sup>a,b,d</sup>, A. Recking<sup>e,d</sup>, A. Burtin<sup>a</sup>, J.-L. Join<sup>a,b</sup>, E. Delcher<sup>a,b</sup>, L. Michon<sup>a,b</sup>, F. Gimbert<sup>d</sup>

<sup>a</sup> Université Paris Cité, Institut de physique du globe de Paris, CNRS, F-75005 Paris, France

<sup>b</sup> Université de La Réunion, Laboratoire GéoSciences Réunion, F-97744 Saint Denis, France

<sup>c</sup> Observatoire volcanologique et sismologique de la Martinique, Institut de physique du globe de Paris, F-97250 Fonds Saint Denis, France

<sup>d</sup> University of Grenoble Alpes, CNRS IRD, Institut des Géosciences de l'Environnement (IGE), Grenoble, France

<sup>e</sup> IRSTEA-ETNA, BP 76, 38 402 Saint-Martin-d'Hères cedex, France

### ARTICLE INFO

#### Keywords:

Seismic noise  
Hydrogeophysics  
Indian Ocean  
Time-series analysis

### ABSTRACT

Monitoring of sediment transport during extreme flood events is difficult and often impossible. Fluvial seismology can provide constraints on the mechanisms of this transport and on the seismic sources but few cases of application in context of extreme events such as tropical cyclones were realized. Recordings from three seismic stations temporarily installed along a river (the Rivière du Mât) located in La Réunion Island (Indian Ocean) are analysed to characterize high-frequency (> 1 Hz) seismic noise induced by the extreme flood generated by the tropical cyclone Dumazile (March 2018). We evidence a good correlation ( $r^2 = 0.94$ ) between the amplitude of the seismic signal and the water level at lower frequencies (2–7 Hz), particularly during the rising limb of the river flood. The relationship between seismic amplitude and water level measurements tested at multiple frequency ranges are consistent with a signal dominated by water flow at lower frequencies and by sediment transport at higher frequencies (15–45 Hz). We show that the use of seismic measurement, particularly at stations located very close to the riverbed can provide comprehensive information on the mechanisms involved during sediment transport associated with extreme flood events when direct measurements are not possible.

### 1. Introduction

La Réunion is a volcanic island located in the tropical part of the western Indian Ocean, about 750 km east of Madagascar (Fig. 1). The island can be impacted by strong atmospheric depressions and tropical cyclones (such as the cyclone Dumazile imaged Fig. 1a and the track of which is shown Fig. 1b), mainly during summer periods, i.e., from November to March, that are able to generate strong winds, swells but also intense rainfalls. Several precipitations world records have been established in La Réunion during such events, like for instance over 72 h (3900 mm) and 96 h (4900 mm) (<http://pluiesextremes.meteo.fr/lareunion/>). Together with steep volcanic reliefs, these hydrological forcings induce very high erosion rates along with rapid landscapes evolution. Preferential incision areas in volcanic rocks produce large sediment transport, making recurrent natural hazards such as floods, banks destruction and landslides permanent challenges for the populations

settled in the vicinity of such areas (Bret et al., 2003; Gayer et al., 2019). During cyclonic floods, the monitoring and the quantification of the river bedload transferred toward the ocean is impossible to achieve via in situ methods such as sediment traps and tracking tracer particles (Wilcock, 1997), due to the strength of the current and to the large size of blocks that can be transported. This motivated the development of indirect observations and the search for proxies such as seismic noise (frequency, amplitude, direction) as it was shown to have direct correlation with hydrological parameters and sediment transport (Govi et al., 1993; Burtin et al., 2008). In this study, we investigate the potential of seismic records to approach and describe fluvial processes in a flooding river during a tropical cyclone.

In fluvial environments, recent studies have shown that the high frequency (> 1 Hz) seismic signals could originate from water turbulence (e.g., Gimbert et al., 2014), waves evolving at the fluid-air interface (Schmandt et al., 2013) and from the river bedload (e.g., Burtin

\* Corresponding author at: Université de La Réunion, Laboratoire GéoSciences Réunion, Institut de physique du globe de Paris, Université Paris Cité, CNRS (UMR 7154), F-97744 Saint Denis, La Réunion, France.

E-mail address: [frfont@ipgp.fr](mailto:frfont@ipgp.fr) (F.R. Fontaine).

<https://doi.org/10.1016/j.jappgeo.2023.105127>

Received 21 July 2022; Received in revised form 6 June 2023; Accepted 5 July 2023

Available online 7 July 2023

0926-9851/© 2023 Elsevier B.V. All rights reserved.

et al., 2008). Apart from these fluvial processes, the ambient seismic energy observed above 1 Hz could originate from numbers of physical processes such as anthropogenic activities (e.g., Eibl et al., 2015), wind (e.g., Boese et al., 2015), rainfall (e.g., Roth et al., 2016; Dean, 2017; Rindraharisaona et al., 2022), volcanic events (McNutt, 1992), ocean waves (e.g., Adams et al., 2002), landslides (e.g., Schöpa et al., 2017), rockfalls (e.g., Deparis et al., 2008) or debris flow (e.g., Arattano, 1999).

Direct observations and numerical models concur that water dynamics dominate the seismic noise at lower frequency than sediment transport (e.g., Burtin et al., 2008; Schmandt et al., 2013; Gimbert et al., 2014; Roth et al., 2016, 2017). Amplitude of the seismic records has been observed to be related to the water level, but the relationship between seismic amplitude and water level does not allow distinguishing sediment transport seismic signature from that of water alone and does not allow yet deciphering the various sedimentary transport processes (sliding, saltation, etc) and water dynamics (turbulence, basal shear stress, vertical pressure variations). Evidences of hysteresis effect have been observed and associated with sediment transport (Burtin et al., 2008; Hsu et al., 2011; Chao et al., 2015) or with complex interaction between water turbulence and river bedload (Gimbert et al., 2014; Roth et al., 2017) and recently demonstrated by direct bedload sampling (Bakker et al., 2020). Frequency-dependent polarization analysis provides also the possibility to locate areas of increased flow turbulence (Goodling et al., 2018).

In this study, we used seismometers deployed in the frame of a regional seismic experiment (data and metadata available at <https://doi.org/10.15778/RESIF.ZF2015>) to constrain the high-frequency seismic signature of a river, the Rivière du Mât, located in the Salazie Basin, on the northern side of La Réunion Island (Fig. 2a and b). From its high overall yearly rainfall (3000 to 5000 mm/y) and its high and steep

topography, the whole northern and eastern part of La Réunion Island is an exceptional region to study fluvial dynamics and sediment transport. The Rivière du Mât drains a 91 km<sup>2</sup> watershed (Fig. 2), with a response time of 4 h (De la Torre, 2008) and torrential characteristics. Its slopes vary between 34% in the upper part and 1.4% downstream. The bed morphology alternates narrow canyons and broader alluvial sections (Fig. 2b).

In the following of the paper, we focus on the measurements obtained during the tropical cyclone named “Dumazile” occurring in March 2018. After presenting the origin of the data and the applied methods, we show the results and discuss the possible origins of the seismic signals, and in particular the signatures of water and sediment transport in light of hydrological, meteorological and sedimentological observations. We finally perform a polarization analysis in multiple frequency bands to describe the ground motion rectilinearity and orientation in an attempt to locate noise sources in time and frequency.

## 2. Framework, data and methods

### 2.1. The Dumazile tropical cyclone

In this study, we focus our analysis on five days of continuous seismic, hydrological and meteorological data covering the Dumazile cyclone event (March 3 to 7, 2018), the track and intensity of which are presented Fig. 1b. This cyclone impacted La Réunion Island with heavy rains (>1500 mm of precipitations over four days). It formed on March 2, 2018 north of La Réunion (Fig. 1b) as a tropical depression. On March 4, the storm was upgraded to tropical cyclone. It was located about 500 km NW of La Réunion and moving southwards. On March 5, 2018, the eye of Dumazile cyclone reached its minimum distance of 400 km west

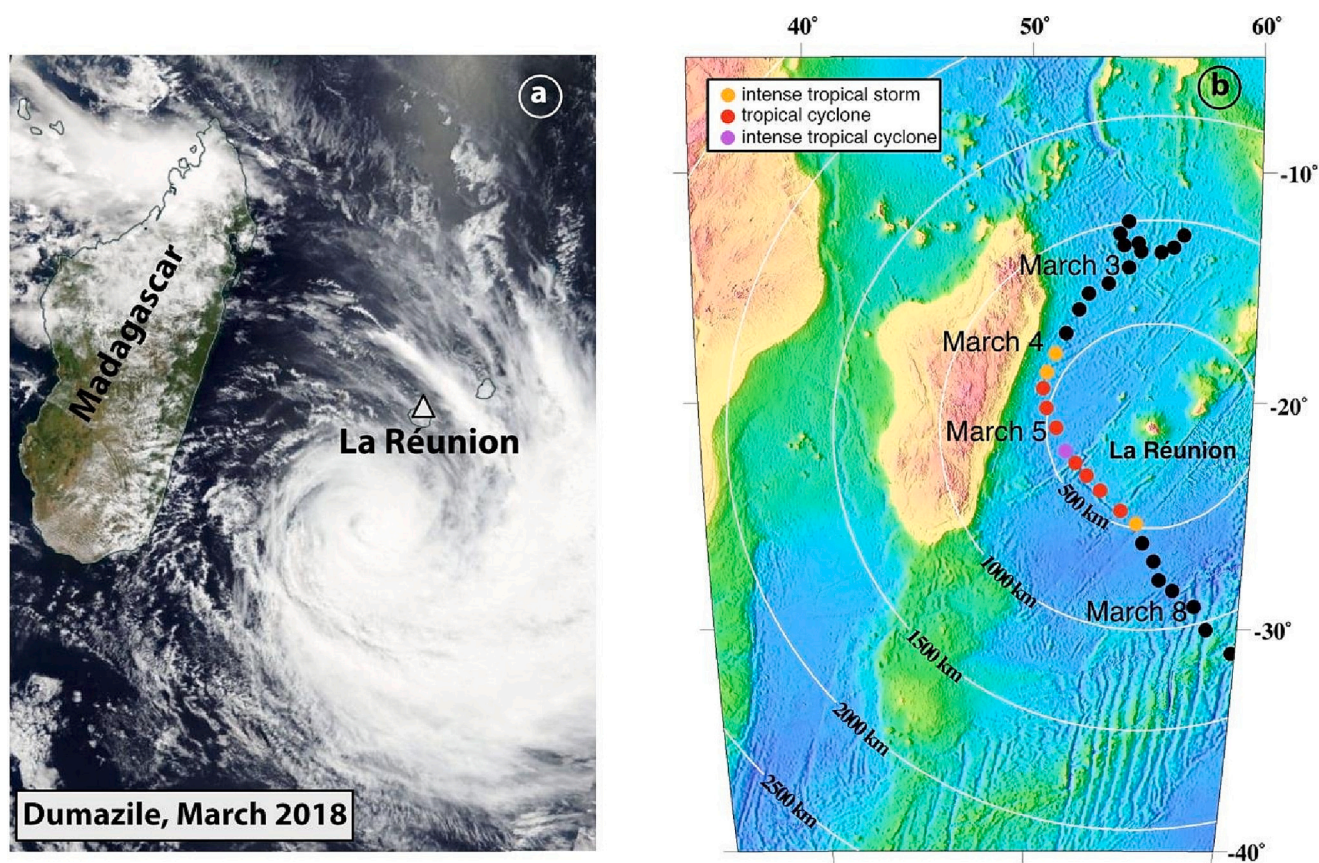
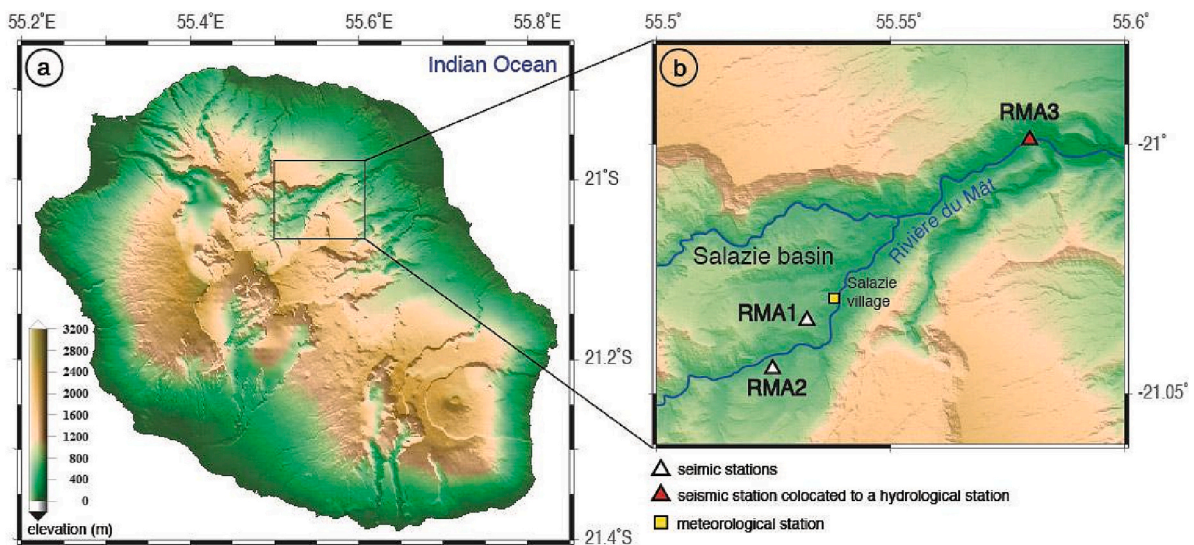


Fig. 1. a) Meteosat-9 satellite image of Dumazile on March 4, 2018 at 05:40 UTC over Madagascar and La Réunion islands (credits: “Météo-France”) showing the size of the cyclone impacting the whole SW Indian Ocean and La Réunion Island in particular. b) Map of the SW Indian Ocean, showing La Réunion Island and the trajectory and intensity (colour-coded) of the cyclone Dumazile (March 4 to 7, 2018). Are also presented circles of the 500 km isodistances centered on La Réunion.



**Fig. 2.** a) Topographic map of La Réunion Island showing the Salazie Basin. b) Detailed map of the Salazie Basin showing the seismic stations (triangles) and the localisation of the water gauge (red triangle) and rain gauge (yellow square). This map was created with the GMT software (Wessel and Smith, 1991) and the digital elevation model of the IGN (<http://professionnels.ign.fr/>, 5-m resolution). (For interpretation of the references to colour in this figure legend, the reader is referred to the web version of this article.)

of the island at 00:00 UTC and attained its grade of intense tropical cyclone at 12:00 UTC (at 440 km from the island). From March 6 to 8, Dumazile decreased in intensity and gradually escaped toward the SE (Météo-France website: <http://www.meteofrance.re/cyclone/saisons-passees/2017-2018/dirre/DUMAZILE>, Fig. 1b).

## 2.2. Material and methods

Three broad-band seismometers RMA1, RMA2 and RMA3 were installed along the riverbed of the Rivière du Mât (De la Torre, 2008) respectively at 500, 350 and 20 m from the riverbed (Fig. 2b). RMA1 and RMA2 stations were equipped with Guralp CMG40 seismometers and RMA3 with a Guralp CMG3-ESPC seismometer. The Guralp CMG40 sensor is characterized by a flat response between 1/40 and 50 Hz whereas the response of the Guralp CMG3-ESPC sensor is flat between 1/120 and 50 Hz. Data were acquired continuously by Nanometrics Taurus digitizers at 100 samples/s which limited our investigations to the Nyquist frequency of 50 Hz (see waveforms on Appendix A1).

Rainfall data (6 min resolution) were extracted from a tipping bucket rain gauge (each tip corresponds to 0.1 mm of rainfall) deployed 800 m downstream from the RMA1 station, in Salazie village (Fig. 2b) and maintained by Météo-France Réunion (<https://publitheque.meteo.fr/>). Water level data (blue curve, Fig. 3) were recorded by a pressure sensor installed in a mobile-bed hydrometric station with a time resolution of 5 min. Interestingly, this sensor was quasi-colocated with the RMA3 station (6.4 km and 7.7 km downstream from RMA1 and RMA2, respectively). The data collected were made available from the “Office de l’Eau de La Réunion” (<https://www.eaureunion.fr/bdd/>).

We computed the power spectral density (PSD, Fig. 3) with a time-frequency analysis using the TiSKIT package developed by W. Crawford (<http://www.ipgp.fr/~crawford/Homepage/Software.html>). The seismic records were first corrected for the full instrument response. This procedure was applied to the seismometer vertical component and with a 60 s moving window and a 50 % overlap. Results are provided in decibel (dB) relative to velocity ( $10 \times \log_{10} [(m/s)^2/Hz]$ ).

We also calculated the average Power Spectral Density (PSD) with the SACPSD software (Herrmann, 2013), over the frequency band 0.01 to 25 Hz before the cyclone on March 3, 2018 (in blue, Fig. 4a, b and c) and during the cyclone, from March 4 to 8 (in red, Fig. 4a, b and c).

To compare hydrological and seismic data, we calculated the root

mean square (RMS) of the seismic vertical component expressed in velocity (m/s). The RMS provides a smoothed measure of the seismic signal amplitude over time and over a given frequency range. We also chose to use the RMS because PSD lowers the highest values of energy due to its unit in dB, issued from the logarithm of the ratio between the energy and the discrete length of the time series. We split our RMS investigations in a Low-Frequency (LF) band and a High-Frequency (HF) band (see Table 1 for specific frequency band at each station): i) to exclude the influence of the primary and secondary ocean microseisms (0.05–0.35 Hz) (Davy et al., 2016) and, ii) to minimize the influence of the main anthropogenic noise likely due to the road traffic (Kuzma et al., 2008) that we observe in our records and that dominates the signal during day-times between about 7 to 15 Hz depending on the station (well visible as broad vertical bands of energy on the spectrograms Fig. 3). Before filtering, we removed the mean value of the signal, removed the trend and applied a 5% Hanning taper. The filtered data of each station was multiplied by the sensor sensitivity (Appendix A2) of each of them as the corresponding instrumental responses of the broadband raw seismic channels are flat in the frequency considered in this study. In these calculations, we used a 30-min average of the RMS to smooth the small peaks to improve the readability (Fig. 5a) and made a 5-min resampling of the RMS time-series to allow calculating the relationship with the water level. In this study, we hypothesize for two reasons that the contribution of rain (Rindrahariasona et al., 2022) to the overall seismic noise amplitude is negligible compared to the influence of river activity:

- Recent studies have shown that the influence of precipitation on the seismic signal is observable above 60 Hz and up to 480 Hz (Roth et al., 2016; Dean, 2017). Dean (2017) particularly observed that the effect of precipitation is strongest above 80 Hz. Whereas the measurements made with the Rivière des Pluies network were limited to frequencies below 50 Hz given the characteristics of broadband seismometers.
- The spectrograms in Fig. 3 do not show a clear correlation between the seismic signal and rain for the two closest seismic stations (RMA1 and RMA2) located at large distance to the river, whereas the seismic signal appears to be strongly correlated to the river water level, particularly at the station RMA3 located close to the river, as discussed below.

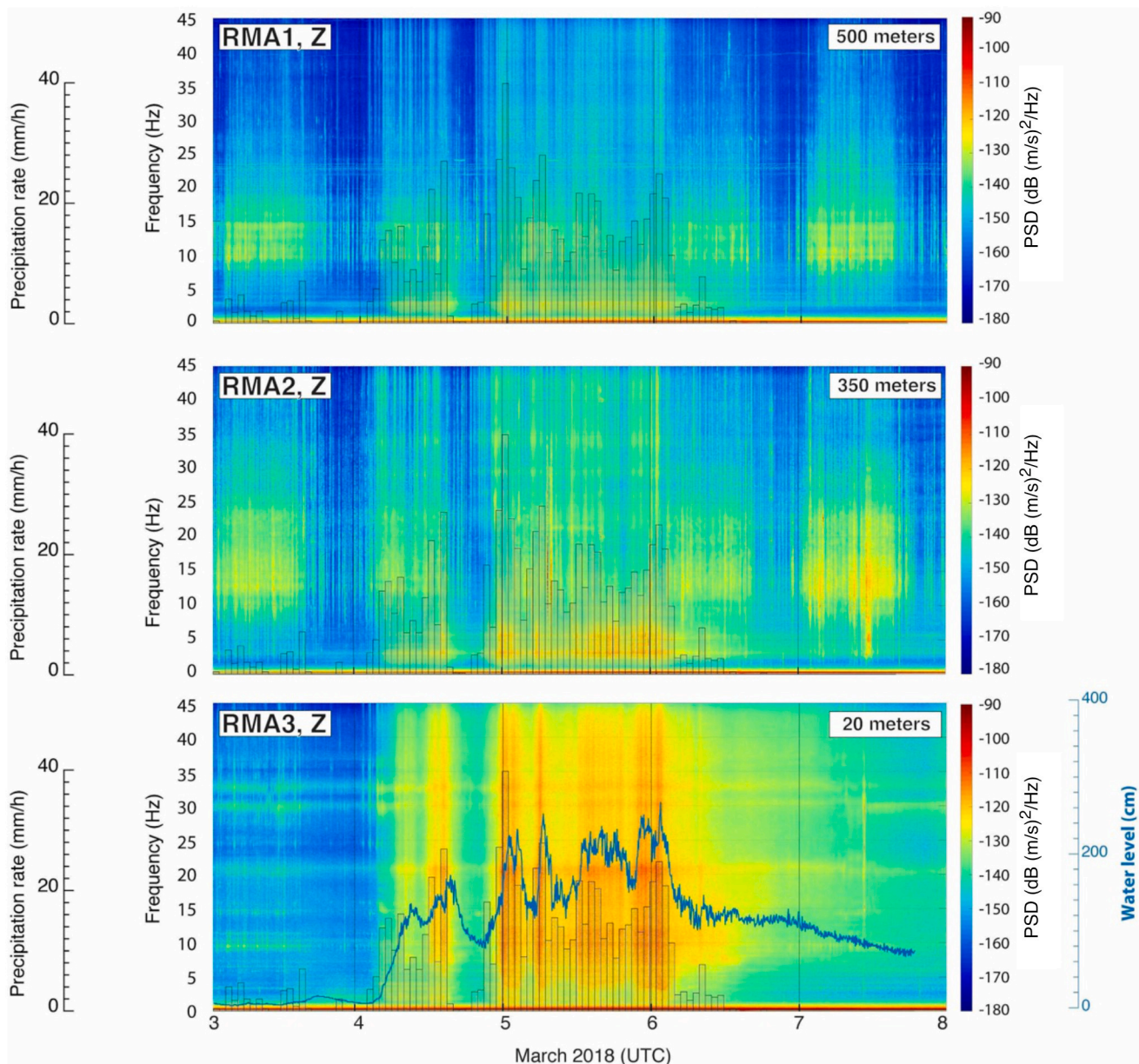


**Fig. 3.** Spectrograms of the vertical-component (Z) continuous seismic record of RMA1, RMA2 and RMA3, during the cyclone Dumazile, from March 3 to 8, 2018, presented with the same colour scale, together with the rain precipitation rate (grey bars). For RMA3, the river water level (blue curve) is also presented to evidence its correlation with the HF seismic signal. The distance to the river is indicated for each station. (For interpretation of the references to colour in this figure legend, the reader is referred to the web version of this article.)

Air pressure changes can load or unload the mass at the Earth's surface inducing near surface variation of seismic velocity (Kramer et al., 2023). The atmospheric pressure measured at the Réunion airport by Météo France ([https://donneespubliques.meteofrance.fr/donnees\\_libres/bulletins/BCA/BCA\\_974\\_2018.pdf](https://donneespubliques.meteofrance.fr/donnees_libres/bulletins/BCA/BCA_974_2018.pdf)) shows a pressure decreases by about 9 hPa as the cyclone approaches from March 5 at 10:00 UTC until March 6 at 17:00 UTC. No simultaneous change of the seismic signals was detected at the 3 stations associated with such change in pressure during the approach of the cyclone and when it is moving away from the island, which suggest a negligible pressure effect.

Diurnal variation temperature was evidenced using dense arrays of seismometers to produce near surface variation in seismic velocity of the order of 0.01% (Mao et al., 2019). However, it is unlikely to explain most of the variation of the seismic signal as the periodic daily or sub-daily signal expected from such effect is not clearly observed.

In order to discriminate and locate possible seismic sources during

the cyclone, we also performed polarization measurements based on principal component analyses (PCA) of ground motion measured by the three-component seismometers, using MatLab codes (Ppol package) (e.g., Fontaine et al., 2009; Davy et al., 2014). This allows retrieving the apparent back-azimuth of the sources in the horizontal plane (the back-azimuth being the direction of the source determined at the recording station) provided at  $\pm 180^\circ$ . The interpretation of the polarization depends on the type of seismic phase considered. Determining all types of seismic waves generated during the period of the cyclone is beyond the scope of this paper and specific numerical models could help to decipher the various types of seismic phases generated at high-frequency. However, it is possible to discriminate *P*, Love and Rayleigh waves from their polarization attributes.

- *P*-waves are longitudinal waves, with quasi-linear polarization. We assume both  $CpZ > 0.8$  and  $CpH > 0.8$  or a value of rectilinearity

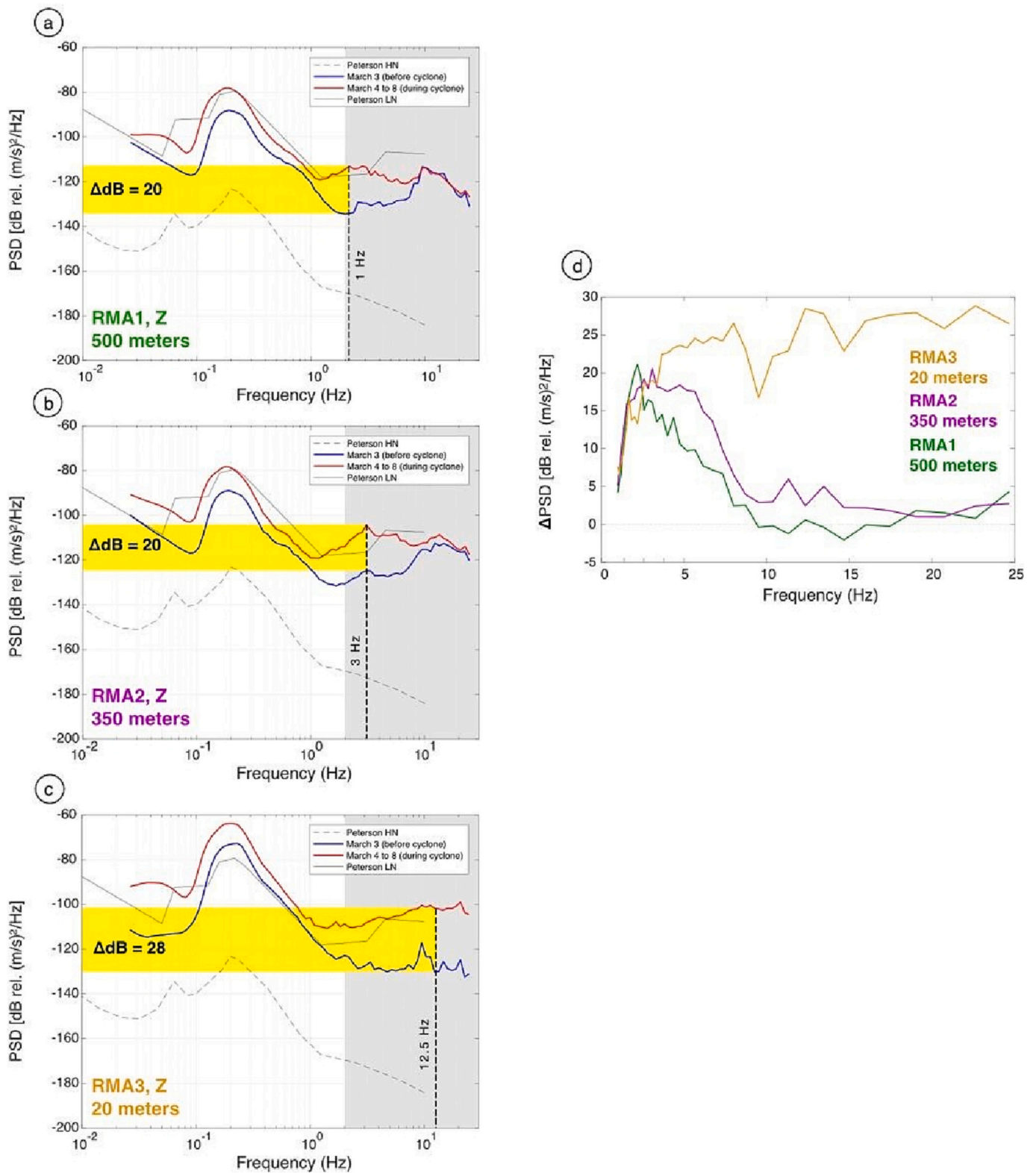


**Fig. 4.** a), b) and c) Average spectra calculated at RMA1, RMA2 and RMA3 respectively before the cyclone (March 3) in blue, and during the cyclone (March 4 to 8) in red, calculated with the SACPSD software (Herrmann, 2013). This representation allows the visualization of the noise variation induced by the cyclone and the flood, at the three sites and over the various frequencies. Solid black line represents the high noise (HN) level model whereas the dashed black curve shows the low noise (LN) level model from (Peterson, 1993). The grey part highlights the 2 to around 26 Hz frequency band. The dotted line indicates the frequency for which the  $\Delta PSD$  is maximum. d) Calculated difference in the noise spectra before and during the cyclone ( $\Delta PSD$ ) for the three seismic stations in the frequency range 1 to 25 Hz, showing the different behaviour depending on the station distance to the riverbed. Note that RMA3 station, located closest to the river display variations of the seismic amplitude over the whole 1–25 Hz frequency band while the two other stations, located at larger distances show only variations in the low frequency band during the flood. (For interpretation of the references to colour in this figure legend, the reader is referred to the web version of this article.)

**Table 1**  
Seismic station coordinates, river-to-station distance and analysed frequency bands at low (LF) and high frequency (HF) for each station.

STATION	Lat. (°)	Long. (°)	River-to-station distance (m)	LF (Hz)	HF (Hz)
RMA1	-21.0352	55.5321	500	2-8	25-45
RMA2	-21.0449	55.5248	350	2-7	20-45
RMA3	-20.9988	55.5797	20	2-7	15-45

higher than 0.8 close to the value (0.9), as used in previous studies (e.g., Bokelmann, 1995; Fontaine et al., 2009).

- Rayleigh waves are characterized by elliptical ground motion and are observed on both longitudinal and vertical components of the seismometer (e.g., Stachnik et al., 2012; Scholz et al., 2017). They exhibit a retrograde ground motion of the Earth’s surface and we assume  $CpZ < 0.5$  and  $CpH > 0.9$  as proposed by Reymond (2010). In the horizontal plane, Rayleigh waves are therefore pointing toward

the source, such as P-waves but show elliptical ground motions in the radial plane.

- Love waves are only present in the horizontal plane and the associated particle displacement is confined along the transverse direction, with a linear polarization. We assume  $CpZ > 0.9$ ,  $CpH > 0.9$  and a vertical polarization angle close to  $90^\circ$  (Reymond, 2010).

SH waves and other type of waves are more difficult to detect from a single seismic station and at high frequencies. It is the case for instance for SH waves also observed on the transverse direction, but with polarization characteristics different to those of P, Love and Rayleigh waves.

The strength of the signal polarization is characterized by the degree of rectilinearity (e.g., Flinn, 1965) measured in the horizontal ( $CpH$ ) and in the vertical planes ( $CpZ$ ). These two coefficients described in Davy et al. (2014) and in Barruol et al. (2016) are equal to 0 for a circular polarization and to 1 for a purely linear polarization (see sketch in

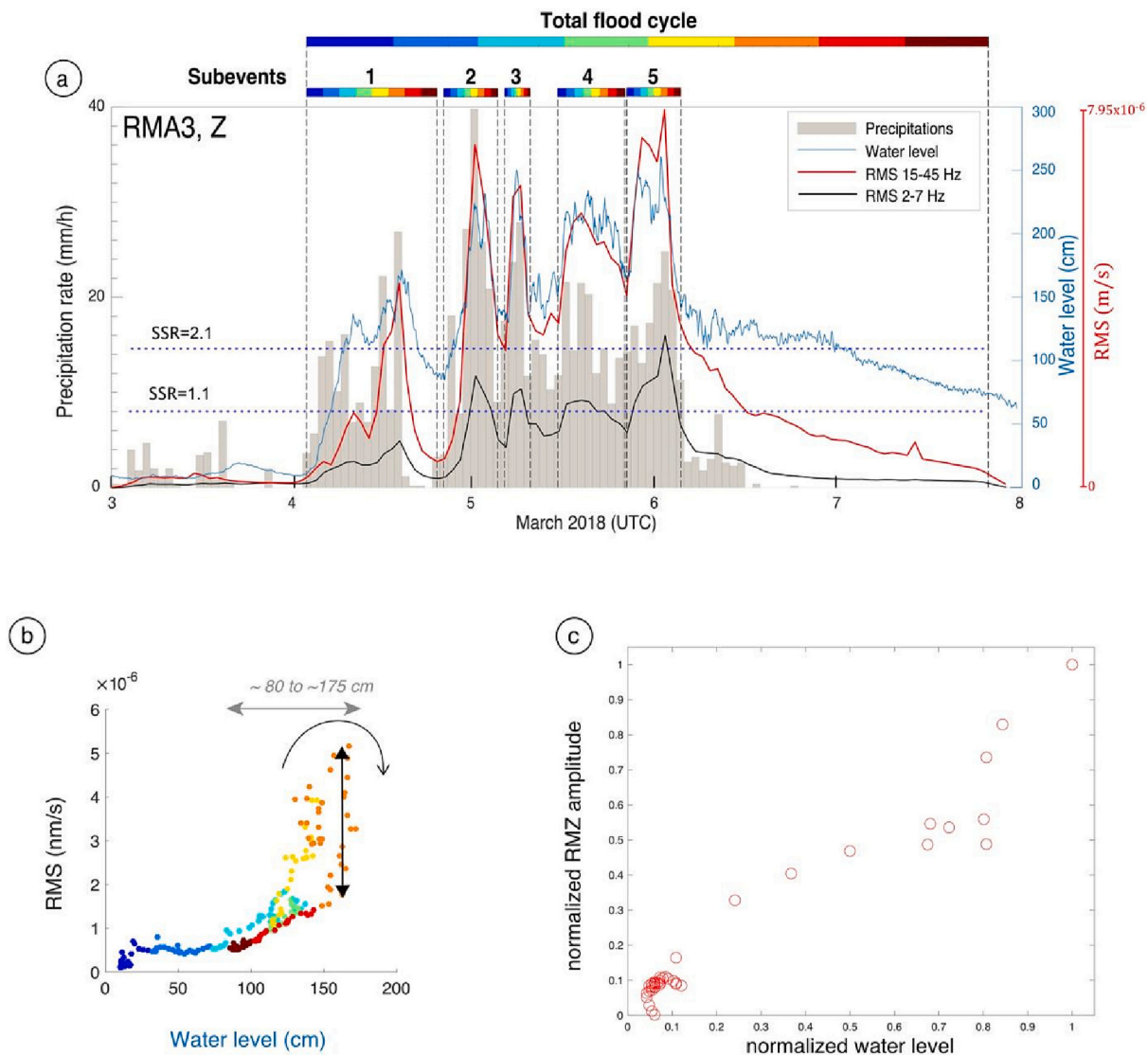


**Fig. 5.** a) Five days’ time-series of hourly precipitation rate (grey bars), water level in the Rivière du Mât (blue line), RMS of the seismic amplitude from RMA3 station in the high frequency band (15–45 Hz, in red) and in the low frequency band (2–7 Hz, in black). Model results of water level threshold are indicated by the two horizontal blue dashed lines (for Shields stress ratio called SSR in this figure  $\tau^*/\tau_c^* = 1.1$  and  $\tau^*/\tau_c^* = 2.1$ ). b) Relationship between water level and RMS of the seismic amplitude in the high frequency band during the only first flood peak called subevent 1 (on March 4). Point colors indicate the time, as the colour bar in Fig. 5a. c) Observed correlation between the hourly RMS amplitude determined in the LF band at RMA3 station and the normalized water level at the same location from March 3 at 00 h00 to the end of the rise associated with the first flood peak. (For interpretation of the references to colour in this figure legend, the reader is referred to the web version of this article.)

Appendix B). More precisely, the polarization coefficients were determined as follow:

$$CpH = 1 - \frac{e_2}{e_1} \quad (1)$$

where  $e_2$  and  $e_1$  are the eigenvalues of the covariance matrix obtained from the two horizontal components with  $e_2 \leq e_1$ .

The apparent back-azimuth of the ground motion  $\theta$  is:

$$\theta = \arctan \frac{u_2}{u_1} \quad (2)$$

where  $u_2$  and  $u_1$  are the cartesian coordinates of  $u$ , the eigenvector corresponding to the highest eigenvalue of the covariance matrix. In the  $E$ ,  $N$  and  $Z$  coordinates system,  $u_1$  corresponds to the coordinate relative to  $E$  and  $u_2$  to the coordinate relative to  $N$ .

We can then determine the longitudinal component  $L$  by  $L = \cos(\theta + \pi)N + \sin(\theta + \pi)E$ ; where  $E$  and  $N$  are the horizontal components. Using the longitudinal and vertical components, we can then determine a third covariance matrix and the degree of rectilinearity of the ground motion in the vertical plane:

$$CpZ = 1 - \frac{f_2}{f_1} \quad (3)$$

where  $f_2$  and  $f_1$  are the eigenvalues of the covariance matrix determined using  $L$  and  $Z$  components and  $f_2 \leq f_1$ .

The coefficient of rectilinearity (Rectilinear) of particle motion in 3D (Jurkevics, 1988) is equal to  $1 - ((\lambda_2 + \lambda_3)/2\lambda_1)$ , where  $\lambda_1$ ,  $\lambda_2$  and  $\lambda_3$  are the eigenvalues of the covariance matrix formed from a principal component analysis applied to the three-component records and  $\lambda_1 \geq \lambda_2 \geq \lambda_3$ .

The vertical polarization angle is obtained with:  $VPA = \cos^{-1}(u_3)$  where  $u_3$  is the Cartesian coordinate of  $u$  the eigenvector corresponding to the highest eigenvalue of the covariance matrix.  $u_3$  corresponds to the coordinate relative to  $Z$  the vertical component.

In order to investigate the possible frequency dependence of the polarization and to separate any possible water-induced signals from sediment-induced signals, data were first filtered in various frequency bands (Table 1). For each band, we used a 1000 seismic cycle-long moving window and a 50 % overlap to bring out the preferential orientation (for example a 222 s time window for the range 2–7 Hz). As shown in Appendix B for  $CpH = 0$  the orientation is not resolved. Therefore, we considered significant polarization measurements when  $CpH > 0.8$  in order to well constrain the orientations and to decrease the uncertainty. The polarization analysis was performed on continuous data spanning March 3 to 7. This window covers the whole Dumazile flood period and includes one day of record before the flood with a water level characterized as low-flow (10 cm at RMA3 station).

### 3. Results

#### 3.1. Noise spectral analyses

Spectrograms of the vertical components of the three seismic stations are presented in Fig. 3, at the same scale, and reveal a clear increase of the overall seismic amplitude of the cyclone, first on March 4 and then on March 5, as the system was increasing in power (upgraded from a tropical storm to a tropical cyclone) and was approaching the island (at distance smaller than 500 km). On March 4 and 5, spectrograms from RMA1 and RMA2 display a PSD increase of 20 dB in the low frequency range (2–7 Hz), while no clear increase is observed at higher frequencies. RMA3 spectrogram also displays a PSD increase of 20 dB in the low frequency range, while a 30-dB increase is simultaneously observed in the high frequency range. Before the cyclone, on March 3, spectrograms show clear anthropogenic noise during day-time, dominating in the 10–20 Hz band, particularly well visible at RMA1 and RMA2. A continuous and stable seismic noise is also observed at RMA3 station at

frequencies around 10, 20 and 30–35 Hz (Fig. 41 from Gonzalez (2019), <https://tel.archives-ouvertes.fr/tel-02468230>). This noise is likely due to anthropogenic activities and might be due to an electric generator for signals with frequency at around 20 Hz, hypothesis which has not been proven yet. There is, however, no evidence of high amplitude signal in both LF and HF frequency ranges during night times at the three stations (Fig. 3), demonstrating that the river, at low flow, produces low seismic noise and that the subsequent noise increase is related to the flood itself. Fig. 3 also presents the precipitation rate (grey histograms) measured at Salazie village (Fig. 2b), located nearly at the centre of the three seismic sites. None of the seismometers was actually colocated with the rain gauge. Such representation therefore assumes that the precipitations are rather homogeneous at the scale of the station coverage during the storm system, which is at first order a reasonable assumption considering the scale of the cyclone (Fig. 1). Going at finer scale, meteorological and climatological studies (e.g., Réchou et al., 2019) show that the precipitation rate is generally stronger on the higher reliefs, i.e., in the middle of the island, where the Rivière du Mât originates (western part of the Salazie Basin). The cumulative amount of precipitations over the time series duration from March 3 to 6, 2018 is therefore likely underestimated and larger than 1500 mm in the upstream part of the Salazie Basin. An apparent correlation between seismic energy and precipitation rate (Fig. 3) is underlined by strongly energetic vertical bands visible on the spectrogram at RMA3 and may suggest a rain-induced seismic noise (physical impact of the droplets on the ground). These bands are however much fainter at the two other sites, hence suggesting that the recorded seismic energy reflects more the water activity in the river rather than the local rain intensity in the very neighbourhood of each site (Dean, 2017; Rindraharisana et al., 2022), assuming the rainfall is rather homogeneous at the scale of the basin. On the spectrogram of RMA3, we also present the water level measured at a quasi-colocated water gauge (blue curve on Fig. 3, bottom). In this case, it makes sense to compare both seismic and hydrological parameters describing the fluvial processes acting at this site of the river. The water level exhibits a correlation with the precipitation rate and also with the seismic noise, as one observes that each peak in the water level generates a clear peak in the seismic noise amplitude.

To better quantify the PSD variation associated with the flood, we present in Fig. 4a, b and c the average spectra computed at each station before (on March 3, blue curve) and during the cyclone (from March 4 to 8, red curve) over the frequency range 0 to 25 Hz. The increase of the PSD during the cyclone is clear in the primary (0.05 to 0.1 Hz) and the secondary (0.1 to ~0.33 Hz) microseismic bands induced by the swell activities in the coastal area and in the ocean basin, respectively (Davy et al., 2016). The spectra also show clear increase at frequencies above 1 Hz, induced by the river flood, that interestingly appears to be modulated by the distance of the seismic station to the riverbed: the closer the station to the river, the larger the seismic amplitudes and variations at high frequencies. To illustrate this feature, we present in Fig. 4d the difference in the noise spectra before and during the cyclone ( $\Delta PSD$ ). At RMA1 (in green Fig. 4d) located at 500 m to the river, we observe a 20 dB noise level variation that occurs at low frequency (around 2–3 Hz) whereas weak variation is observed at higher frequencies ( $> 10$  Hz) before and during the flood. At station RMA2 (in purple Fig. 4d) located 350 m from the riverbed, we also observe a clear 20 dB noise increase. High  $\Delta PSD$  values spread at slightly higher frequencies (2 to 7 Hz), however we still observe the absence of clear noise variation at higher frequencies. The observations made at these two stations suggest the effect of the distance, attenuating preferentially the high frequencies emitted by the river activity. At station RMA3 located at proximity of the river (20 m), we observe a very different pattern, with a strong noise variation (20 to 28 dB) over a much wider frequency range (from 2 to 45 Hz) indicating a clear flood signature over the whole spectrum.

### 3.2. Connecting seismic, hydrological and meteorological data

In Fig. 5 we compare hydrological and meteorological parameters to the RMS of the vertical seismic component of station RMA3 filtered in the LF (black curve) and HF bands (red curve) (as defined Table 1). The water level time series (blue curve, with 5 min resolution) has been averaged (sliding mean value) over 15 min in order to minimize the short time variations of noise generated by the very local waves. As already shown on the spectrogram Fig. 3, the precipitation rate (grey histogram) and the water level covary, indicating that the water level is a good proxy for the local rainfall over the upstream part of the basin.

The Fig. 5a and c highlight the good correlation ( $r = 0,97$  for LF and  $r = 0,89$  for HF) between the amplitude of the seismic signal at RMA3 station 20 m from the stream, and the water level, which is well visible at both LF (2–7 Hz,  $r^2 = 0,94$ ) and HF (15–45 Hz,  $r^2 = 0,80$ ). We computed the  $p$ -value (probability of obtaining this correlation coefficient value by random chance) to assess the significance of the fit during the first rise. The correlation coefficient is statistically significant for a level of significance of 1% at both LF and HF with  $p$ -values  $< 0,001$  at both LF and HF. Fig. 5c highlights the good correlation between the RMS amplitude and the water level in the LF band. Fig. 5a also shows that the amplitude of the RMS filtered between 2 and 7 Hz (black curve) is more than twice lower (max  $\sim 3 \times 10^{-6}$  m/s) than the RMS filtered between 15 and 45 Hz (max  $\sim 8 \times 10^{-6}$  m/s).

We cut out the whole period of Dumazile cyclone in five short-duration precipitation and flood subevents about ten hours long (Fig. 5a), each characterized by an individual pulse of precipitation, associated to a sudden increase in the water level and in the seismic noise amplitude. During the first event, hereafter called “subevent 1” (Fig. 5a), the maximum precipitation rate that reaches almost 28 mm/h falls abruptly down to 0 mm/h within an hour, while the water level decreases from 1.8 to 0.9 m. Simultaneously, the RMS between 15 and 45 Hz (red curve) declines from  $3,5 \times 10^{-6}$  to  $0,5 \times 10^{-6}$  m/s within an hour, while keeping a good correlation of  $r^2 \sim 0,89$  with the water level during this step. The maximum precipitation rate (40 mm/h) occurs on early March 5 (subevent 2) and corresponds to a clear peak of the seismic amplitude in the two frequency bands.

After the last progressive decrease of the rainfall rate associated with the Dumazile cyclone event (on March 6, 00:00 UTC, subevent 5), both seismic amplitude and water level signals decrease (Fig. 5a), but at different rates. The seismic RMS curves both display a rapid decrease and reach their initial amplitudes on March 8, in advance of the water level, signing a clear hysteresis, marked by the fact that a given water level did not generate a seismic noise of similar amplitude at the beginning and at the end of the cyclone-induced flood.

The seismic amplitude in the LF range increases as soon as the water level rises (with successive changes of slope at 45, 80 and 120 cm of water height) (Fig. 5a). Assuming that coarse sediment transport does not start immediately, this is consistent with a control of these low frequencies in the seismic records by the water flow turbulence (Burtin et al., 2011; Gimbert et al., 2014; Nanni et al., 2020). Interestingly, the HF band shows a contrasted behaviour: the seismic signal remains very weak (see the starting blue horizontal line in Fig. 5b) until the water height reaches  $\sim 80$  cm. It subsequently increases at higher rate when the water height reaches 120 cm.

For both LF and HF bands in the middle of the first subevent, the amplitude of the seismic signal drops suddenly for a water level of  $\sim 160$  cm, this latter remaining constant. During this stage, the seismic sources appear to be switched off, but do not fall back to the initial noise level at low flow. During this decline phase, the RMS in both frequency bands decrease rapidly with the water stage (indicated by the vertical double arrow Fig. 5b for the HF band), at a rate similar to the rising rate just before the drop. We will see in the following discussion that these thresholds observed in the seismic signal are consistent with what can be expected for bedload transport, for such flow conditions.

### 3.3. Polarization analyses

Polarization measurements of the three component seismic data were performed at the three seismic stations during the Dumazile cyclone period, in both the low (LF) and high (HF) frequency bands and are presented Fig. 6 for RMA3 (Fig. 6a and b, Appendices C, D1 and D2), RMA2 (Fig. 6c and d) and RMA1 (Fig. 6e and f). For each station, we present in blue the evolution of the coefficients of rectilinearity in the horizontal ( $CpH$ ) and vertical plane ( $CpZ$ ), in the LF and HF bands, as defined in Table 1 and in red the back-azimuths of the seismic sources. In the following of the discussion, we consider that a  $CpH$  (or  $CpZ$ ) lower than 0.5 indicates a weakly elongated ground motion ellipsoid averaged over the measurement window and that the signal becomes linearly polarized for  $CpH$  (or  $CpZ$ ) larger than 0.8 (see sketch in Appendix B).

In the case of RMA3, the closest station from the riverbed (20 m),  $CpH$  displays very different behaviour in the LF and HF bands relative to the water level measured at the same site before and during the cyclonic flood. At low frequency (2–7 Hz) and before the first water level increase (Fig. 6a), the  $CpH$  are very scattered and then becomes low while the  $CpZ$  is slightly higher (0.6) but becomes also weak (0.3), suggesting no polarization in both horizontal and vertical planes. During the flood starting on March 4, 2018, we observe that the water level is well correlated to both the  $CpH$  and  $CpZ$  parameters that display similar variations and that reach high values ( $> 0,8$ ) at each flood peak except the first one. The simultaneous elongation of the ground motion in both horizontal and vertical planes, correlated with the water level, indicates that each flood peak generates an approximately linear and horizontal ground motion, that could be schematized by an elongated ellipsoid in the horizontal plane, similar to what could be expected for horizontally-propagating compressive waves but also for horizontally-propagating Love waves. For all flood peaks except the first one, both  $CpH$  and  $CpZ$  values higher than 0.8 are observed indicating a linear polarization. The vertical polarization angle is close to  $90^\circ$  suggesting a nearly horizontal polarization, compatible with either Love or  $P$ -waves. In the case of  $P$ -waves, the circular mean back-azimuths during these peaks trend  $N335,0^\circ E \pm 1,7^\circ$  (the circular standard deviation), i.e., toward a narrowing part of the river in the very vicinity of the seismic station (cf. aerial photograph Fig. 7). In the case of Love waves, the source should be at  $90^\circ$ , i.e. along azimuths of  $N245^\circ E$  or  $N065^\circ E$  (due to the  $180^\circ$  ambiguity), i.e. toward the linear segment of the river east of the station. Using a single 3 component station cannot allow to discriminate among these two hypotheses.

At RMA3 in the high frequency band (15–45 Hz) (Fig. 6b), the polarization appears to behave differently: before the beginning of the rise associated with the first flood peak, we observe seismic phases with both  $CpZ > 0,9$  and  $CpH > 0,9$ , that could suggest  $P$ -waves (e.g. Bokelmann, 1995; Fontaine et al., 2009) pointing toward back-azimuths of  $N255,6^\circ E$  with circular standard deviation = 1.4. The preferred direction of the ground motions is therefore similar to the flow direction (around  $256^\circ E$  at the closest point to the seismic station corresponding to a narrowing of the river bed) suggesting longitudinal waves and thus the presence of  $P$  waves (See for instance on March 3 on Fig. 6b).

Then, we observe a strong decrease of both  $CpH$  and  $CpZ$  (well below 0.5) associated to the flood peaks, indicating an overall loss of polarization. This strong decrease of the overall rectilinearity of the ground motion suggests the presence of several and simultaneous individual sources along the riverbed, emitting signals in a wide range of back-azimuths, resulting in a quasi-circular ground motion in the two planes. Such signal may reflect the displacement of boulders along the river bed during the flood, interacting together and generating HF signals all along the river bed. The hydro-sedimentary interpretation of this phenomenon will be addressed in the discussion below. We furthermore do not observe any correlation with the water level from that moment.

At stations RMA2 and RMA1, located respectively at 350 and 500 m to the river, one observes similar polarization patterns in the HF band (Fig. 6d and f), with important scattering of both  $CpH$  and  $CpZ$ , with

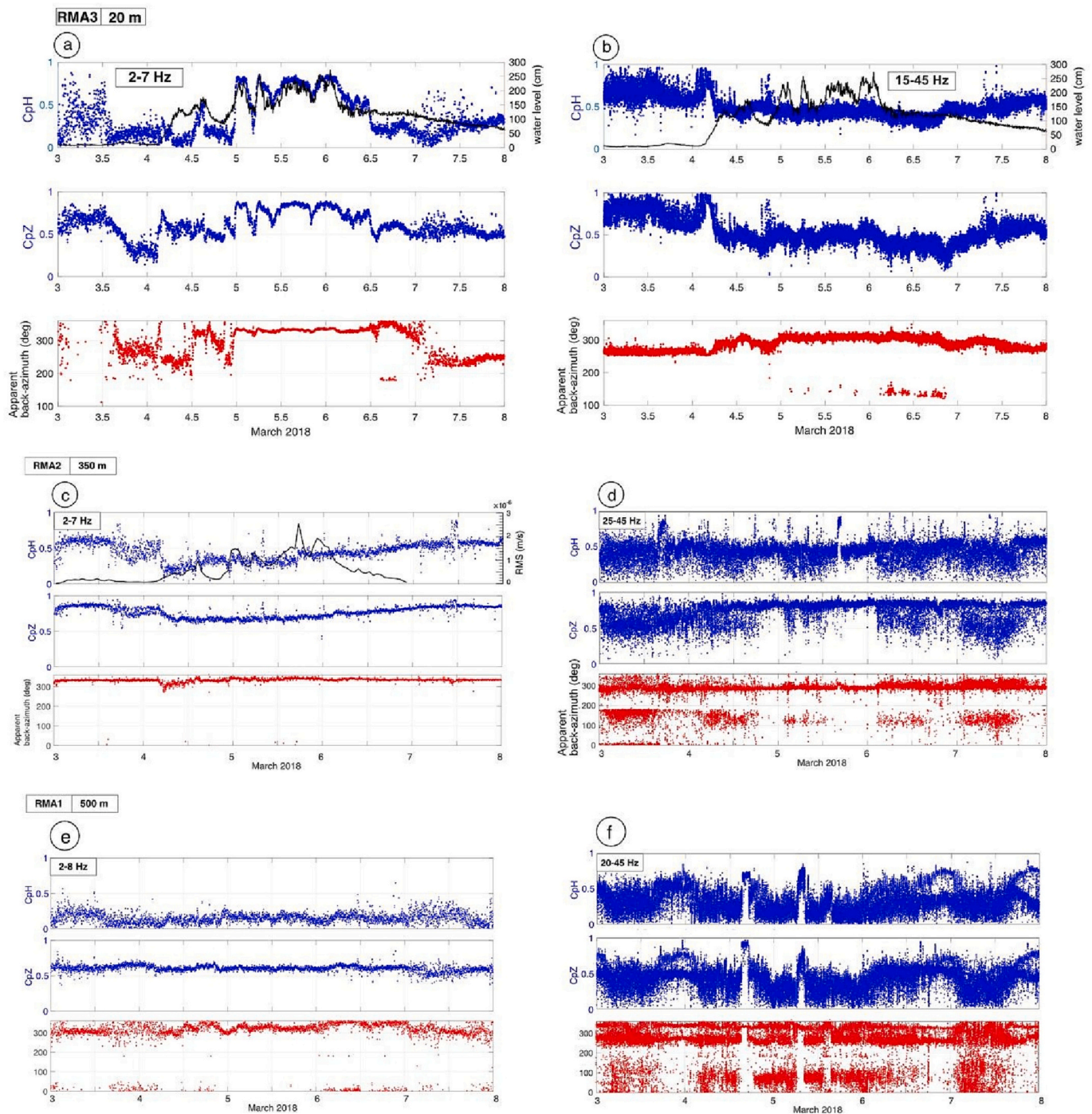


**Fig. 6.** Results from the polarization measurements performed at RMA3 (a and b, upper row), RMA2 (c and d, middle row) and RMA1 (e and f, lower row), in the low frequency band (left column) and in the high frequency band (right column), from March 3 to March 8, 2018, during the cyclone Dumazile. The frequency bands are indicated on each plot. For each station are presented the  $CpH$  and  $CpZ$  (in blue) and the measured back-azimuth (in red). For RMA3 is also plotted the water level (in black) and the RMS at RMA2 for the comparison. (For interpretation of the references to colour in this figure legend, the reader is referred to the web version of this article.)

little variation in time and without any correlation with the cyclone activity nor with the water level in the river. Polarization is weak at the two sites, with slightly higher coefficients at RMA2 ( $CpH \sim 0.5$  and  $CpZ \sim 0.7-0.8$ ) than at RMA1 where both  $CpH$  and  $CpZ$  vary between 0.1 and 0.6. These weakly polarized signals therefore prevent any reliable interpretation of the back-azimuth values.

In the LF band, polarization at RMA2 (350 m from the stream) display a clear decrease in both  $CpH$  and  $CpZ$  on March 4, 2018, and then a slight but continuous increase of the two parameters, but no

correlation with the RMS in the LF (2–7 Hz, black curve, Fig. 6c) that could represent a good proxy of the water level. The slightly higher values of  $CpZ$  (0.6 to 0.8) than  $CpH$  (0.2 to 0.5) indicate a ground motion dominantly in the horizontal plane but with little (but constant) elongation. These  $CpH$  values imply not well resolved azimuths during the flood.

In the same LF band at RMA1 (500 m from the stream), the very low  $CpH$  (0.1 to 0.2) and higher  $CpZ$  (0.5 to 0.6) indicate a quasi-circular ground motion in the horizontal plane, and therefore, little



**Fig. 7.** Map of the surrounding area of the seismic stations RMA3 (yellow triangle) relative to the Rivière du Mat. The blue arrow indicates its flowing direction. The two preferred orientations obtained at LF (2–7 Hz) during the flood and at HF (15–45 Hz) just before the flood are represented in yellow and red, respectively. The solid yellow line corresponds to the expected orientation for *P* waves whereas the yellow dashed line is the direction in the case of Love waves. The uncertainty on each preferred orientation is shown in pink. The yellow triangle represents the RMA3 station location and the red square shows the location of the mobile-bed hydrometric station that was recording with a time resolution of 5 min. (For interpretation of the references to colour in this figure legend, the reader is referred to the web version of this article.)

significance of the resulting measured azimuths (Fig. 6e).

This polarization analysis clearly evidences a decrease of polarization strength with distance to the river, likely produced by the simultaneous presence of multiple noise sources emitting from various back-azimuths. It shows, however, that this technique may be helpful in detecting noise sources and in characterizing processes, as soon as the station is close to the river.

## 4. Discussions

### 4.1. Characterization of sediment transport

Recent field analyses have demonstrated that the seismic power considered in the high frequency band (~20–30 Hz) can be used as a relevant proxy for bedload transport (Bakker et al., 2020). On the basis of this result, let us discuss the high frequency RMS shown in Fig. 5 as a proxy for bedload transport at RMA3.

We can distinguish several subevents, from which we can make several observations:

- Before subevent 1 (March 3): the water level is low, and the HF RMS is close to zero
- Start of subevent 1 (March 4 at ~5:00): a water level of approximately 60 cm corresponds to a sudden increase of the HF RMS. Because the HF RMS reaches zero again at the same water level on March 8, we can infer  $h = 60$  cm as the condition for bedload incipient motion.
- First part of subevent 1 (March 4, ~ 5:00 to 09:00): as the flow increases, the HF RMS increases slowly and reaches values much lower than what is observed in the rest of the signal for similar water level (compare with March 6 near 07:00). This low response is consistent with a low transport due to bed armouring (Bathurst, 2007).
- Middle of subevent 1 (March 4, at ~10:00): a sharp HF RMS increase is observed at a water level of approximately  $h = 110$  cm. We will see

in the next section that this water stage is consistent with the condition for the armour layer destabilization.

- Second part of subevent 1 (March 4, ~10:00 to 14:00): the HF RMS continues to increase with the water level, up to maximum water level at 160 cm.
- End of subevent 1 (March 4, ~15:00 to 20:00): one observes a sudden drop of the RMS signal. Intriguingly, this drop precedes the water stage recession by about 2 h. Even if we cannot conclude on the physical process concerned, it is worth noting that this observation is very consistent with recent flume observations of the seismic response of self-generated bedload pulses (Piantini et al., 2021). In all runs performed in this experimental study, the high seismic power associated with the propagation of the pulse was observed to be systematically dumped to near zero each time bedload propagates over a moving carpet of fine sediments, despite the transport rates is maintained high. This flume result can help to interpret our field observation. After armour breaking the bed subsurface material is not protected anymore and can be remobilized by the flow (Lenzi et al., 2006; Turowski et al., 2009; Recking, 2012), and the sudden drop of the signal to zero could be interpreted as a wash out of the bed material near RMA3 when the flow increases at  $h = 160$  cm.
- Subevent 2 to 5: the RMS is high and closely matches the water level evolution for the rest of the flood. This could be explained by the fact that once the subsurface gravel mixture has been washed out by the first flows, the transport of loose large stones over bedrock generates stronger seismic power.
- After subevent 5: the RMS signal decreases rapidly, which can be explained by less material available for transport. It is responsible for hysteresis in the discharge bedload relation.

From this signal analysis we extracted two particular water stages,  $h = 60$  cm and  $h = 110$  cm, that we associate respectively to incipient motion and armour breaking conditions. We tested these hypotheses by computing the Shields stress  $\tau^*$  and the critical Shields stress  $\tau_c^*$  for the

considered flow conditions: bedload starts when  $\tau^* = \tau_c^*$  and armour breaking is usually considered when  $\tau^* \approx 2\tau_c^*$  (Wilcock and Mcardell, 1993; Church et al., 1998; Recking et al., 2009). The Shields stress is:

$$\tau^* = \frac{hS}{(s - 1)D} \tag{4}$$

Where  $S$  is the bed slope,  $s = \rho_s/\rho$ ,  $\rho_s$  being the sediment density,  $\rho$  the water density, and  $D$  the grain diameter. The surface grain diameters  $D_{50} = 70$  mm (i.e. the median grain size) and  $D_{84} = 180$  mm (size for which 84% of the particle size distribution is finer) were measured in the field (with a Wolman count (Wolman, 1954)) at station RMA3 (Fig. 8). The grain size was measured 1.3 km downstream of the RMA3 seismic station (where the bed was accessible), close enough (when compared to the total 35 km river length) to be representative of the coarse mixture present in this part of the stream, with no visual evidence of downstream fining. Because the seismic response of the bed is more likely due to the large stones (Tsai et al., 2012), the diameter  $D_{84}$  is considered. This diameter was also found to be more relevant for characterizing the bed mobility (Recking, 2010; MacKenzie et al., 2018). Consequently  $\tau_c^*$  is computed with a formulation derived for  $D_{84}$  (Recking, 2009):

$$\tau_{c,D84}^* = 0.56S + 0.021 \tag{5}$$

Using these data with an average bed slope  $S = 1.72\%$  at RMA3, we can compute  $\tau^*$  and  $\tau_c^*$  for the considered flow depths  $h$ . Results are given in Table 2.

We conclude that the two water depths  $h = 60$  cm and  $h = 110$  cm are consistent with the conditions for incipient motion and armour breaking respectively, which supports the above signal interpretation.

We associated one additional flow depth  $h = 160$  cm to the sudden RMS decrease, which we interpreted as a washout of the bed material. This flow depth corresponds to a Shields stress  $\tau^* = 0.09$ , which is about  $3 \times \tau_c^*$ , and in terms of bedload transport, is located above the Shields stress for full bed mobility  $\tau_m^*$  as it was defined from the analysis of available field and flume data sets (Recking et al., 2016).

Because direct bedload monitoring will for long be impossible in such tropical flood, only indirect evidences or proxies offer the possibility to discuss the relation between seismic power and bedload

**Table 2**

Bedload transport calculations results for different values of  $\tau^*/\tau_c^*$ .  $\tau_c^*$  obtained from Eqs. (5) and water depth ( $d$ ) from Eq. (4).

	$h = 0.6$ m	$h = 1.1$ m
$\tau^*$	0.034	0.064
$\tau_c^*$	0.030	0.030
$\tau^*/\tau_c^*$	1.1	2.1

transport. In that sense, the results presented here match qualitatively and quantitatively what could be expected in the different steps of a flood event: start of transport, armour breaking, sediment wash out, and sediment starving at the hydrograph recession. These results support the hypothesis of a HF RMS signal primarily controlled by bedload transport, but only repeated field survey of tropical floods could help to conclude.

#### 4.2. Influence of the river-to-station distance on the water and sediment seismic signature

The observation of strong noise variation (20 to 25 dB) over a wide frequency range (5 to 45 Hz) at RMA3 station (Fig. 4d) clearly demonstrates that the high-frequency part of the noise is more successfully recorded in the direct vicinity of the river. Such dependence of the noise amplitude and frequency content to the river-to-station distance suggests that high-frequencies are strongly attenuated with distance, as already described by Burtin et al. (2011) from seismic observations and modelled by Gimbert et al. (2014). In their study, Gimbert et al. (2014) modelled indeed the PSD values expected for both the water turbulence and the sediment transport for two different river-to-station distances: 100 and 600 m. In their models, a station installed at 600 m from the riverbed should be characterized by a noise dominated by water flow turbulence signature at low frequencies (3–8 Hz), while the grains impacts should sign at slightly higher frequencies, dominantly in the 10–18 Hz frequency band, the higher frequencies being more strongly attenuated over the distance. Our seismometers located at distances ranging from 20 to 500 m to the riverbed provide the opportunity of comparing the observed noise levels to those theoretical predictions. We

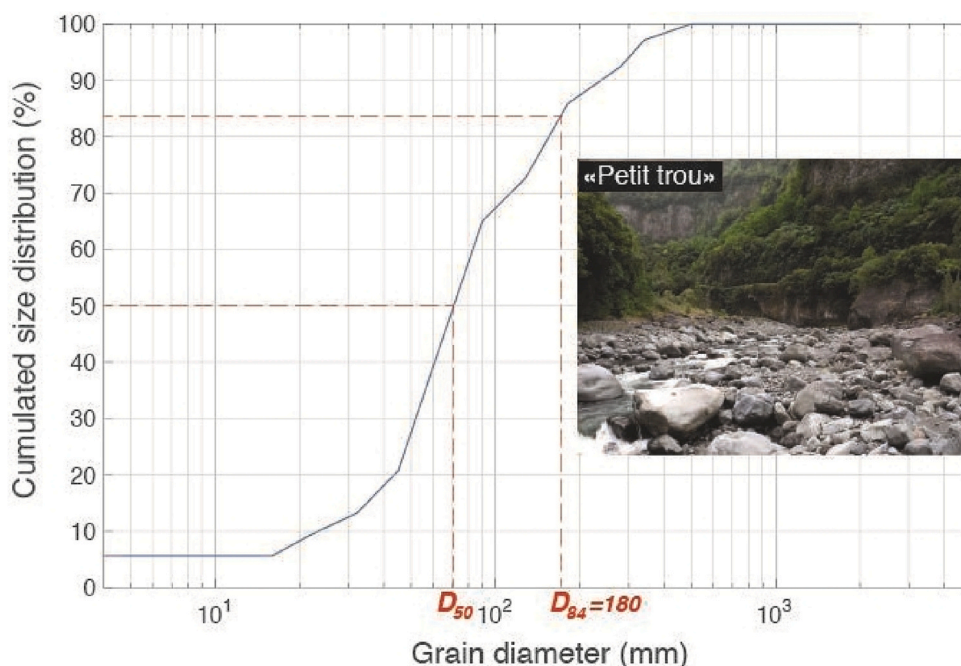


**Fig. 8.** Grain size distribution curve of the sediment sampling at the site called “Petit trou”, 1.3 km downstream the seismic station RMA3, issued from a Wolman count. On the right of the graph is a picture of the river section (upstream view). Are presented on the graph the  $D_{50}$  and  $D_{84}$  distributions used in the text.

computed the theoretical values for the Rivière du Mât (Salazie) setup: a water flow depth  $h = 2.7$  m, a channel width  $W = 20$  m, a riverbed slope angle  $\theta_{river} = 1.72^\circ$ , a median size of riverbed grains  $D_{50} = 0.070$  m, a bedload flux  $q_b = q_{bc}/5$ , where  $q_{bc}$  is the bedload flux at transport capacity calculated following Fernandez Luque and van Beek (1976) as used in Gimbert et al. (2014) for the Trisuli River, a standard deviation of the log-raised cosine distribution of 0.10 and a quality factor  $Q = 50$  as used by Battaglia and Aki (2003) for surface waves in Piton de la Fournaise volcano. Interestingly, the results from this modelling (Fig. 9) is supporting the observations from this study of high-frequency signals related to bedload transport and low-frequency signals associated with water turbulence. At our stations RMA1 and RMA2, the high frequency noise has indeed much smaller amplitudes than RMA3. This agrees with the model predicting that the bedload signature should spread over a larger frequency domain (starting at lower and ending at higher frequencies) at seismic station closer to the riverbed and that its amplitude would dominate the flow turbulence signature. RMA3 station installed at 20 m from the riverbed clearly confirms the presence of strong energy spread from low to high frequencies, as shown in spectrograms Fig. 3 and in average spectra Fig. 4c and d. In case of a station very close to the riverbed, one likely records the signature of the bedload transport over most of the spectrum. Therefore, our observations support the model predictions of Gimbert et al. (2014) and Tsai et al. (2012) even though their model use different input than our own parameters (fluvial settings, attenuation, etc.) and used assumptions of the type of sediment transport (i.e. saltation suggesting Rayleigh-waves). Other observations also dissociate water flow from bedload transport (e.g., Burtin et al., 2008, 2011; Schmandt et al., 2013), assigning water flow seismic signature to lower frequencies than bedload transport, as was recently confirmed by subglacial hydrology that clearly attributes low frequency noise (in the 3–7 Hz) to water flow (Nanni et al., 2020).

#### 4.3. Seismic sources of noise from polarization analysis

Polarization analysis is a powerful approach to analyse three-component signals and to locate seismic sources, since it may help to discriminate a dominating single noise source from the presence of simultaneous different sources. It may also provide information on the nature of the seismic waves that may explain the characteristics of the

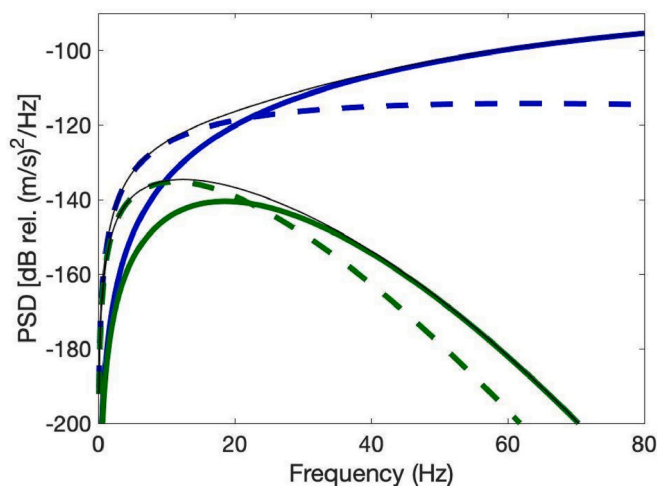


Fig. 9. Predicted PSD values in this study for the Rivière du Mât (Salazie) parameters from the water turbulent flow model (Gimbert et al., 2014) (thick dashed lines) and for the bedload source (Tsai et al., 2012) (thick continuous lines). PSD values for these two models are shown for two distinct distances: 20 m (in blue) and 500 m (in green). Thin solid lines represent the sum of the PSD predicted by both models at two distances. (For interpretation of the references to colour in this figure legend, the reader is referred to the web version of this article.)

observed ground motion.

As already concluded above, for polarization analysis, it is necessary to take into account the distance of the station to the river. The farthest stations RMA1 (500 m) and RMA2 (350 m) do not allow us to identify fluvial signal among the numerous other seismic sources at high and low frequencies, as we observe low and highly dispersed  $CpZ$  and  $CpH$ .

Only station RMA3, the closest to the riverbed (20 m), shows polarization at low and high frequencies that appears to be responsive to fluvial activity. As seen previously in the RMS time series presented Fig. 5, the HF, likely sediment-induced noise is higher in amplitude than the LF, flow-induced noise, indicating that one has potentially access to the flow signature only when the sediment is not transported, i.e., at low water stage.

At station RMA3 and at low frequency, the very similar variations of our polarization measurements (Fig. 6a) with the water level before and during the cyclone and the estimated dominant back-azimuths ( $N335^\circ E$  for a  $P$ -wave or  $N065^\circ E$  for a Love wave) suggest an origin associated with either water flow and the shrinking of the river bed in front of the seismic station or a source toward the linear segment of the river east of the station. We interpret these polarization observations as a dominant water flow influence in the seismic noise at LF, particularly at high water level. At high frequency, the polarization of the signal in the horizontal plane evolves with the same pattern as water level only until it reaches 120 cm during the second flood event. It is then followed by a sudden drop of  $CpH$ . This abrupt change in polarization in this HF band occurring at the early of March 4 coincides for RMA3 with the starting of sub-event 1 and could be related to the bed armour breaking. Before such breaking event, the channels are generally very marked and sediment transport follows preferential paths imposed by macroforms. At the breaking of the bed armour, the macroforms fade and the sediment transport is generalized over the entire river bed. Furthermore, before the breaking, an alluvial mattress is present and the shocks are rather concentrated on hard points (wall, blocks, etc.). After the rupture and evacuation of the alluvial mattress, shocks occur everywhere on the bedrock. We interpret this stage as a possible threshold in the river dynamics when sediments transport may start dominating the seismic noise. From our bedload transport calculations (Shields number), we propose that the water level of 120 cm (corresponding to  $\tau^*/\tau_c^* \sim 2.1$ ) indicates a threshold for the mobility of the coarse bed material just after armour breaking. Again, this interpretation is consistent with models from Gimbert et al. (2014) which predict sediment transport to be associated with a higher frequency content of the seismic noise than the water flow.

During the flood peak, seismic signal at station RMA3 in the HF band (15–45 Hz) shows a weak  $CpH$ , and therefore an absence or weak preferential orientation pointing toward a dominant noise source. This can be easily explained by the fact that the whole river segment in the vicinity of this station is emitting simultaneously seismic signals. Seismic record at RMA3 is therefore composed of multiple point sources spread along the river and therefore arriving at the station with a wide range of back-azimuths, the sum of which making the overall signal almost isotropic. On the contrary, the low frequency band (2–7 Hz) dominated by water flow shows a stronger polarization at higher water level and vice versa, suggesting a very local source signature induced by the water flow.

## 5. Conclusion

In this study, we analysed seismic records in the 1 to 45 Hz frequency range at three broadband three-component seismic stations located along a mountain stream in La Réunion Island during a tropical cyclone, together with hydrological and meteorological data. A good correlation is observed at both low (2–7 Hz) ( $r^2 \sim 0.94$ ) and high frequency bands (15–45 Hz) ( $r^2 \sim 0.80$ ) between the seismic amplitude and the water level in the river during the cyclone-induced flood, confirming that the seismic amplitude at high frequency (>1 Hz) can be used as a good

proxy of the water level during such extreme event. Furthermore, we extracted two particular water stages,  $h = 60$  cm and  $h = 110$  cm from the signal analysis of our closest seismic station, that we associate respectively to bedload incipient motion and armour breaking conditions, which is consistent with bedload transport calculations.

Polarization techniques have been used and helped us discriminating the different physical processes. Polarization measurements at the station very close to the river indicate that the low frequencies ( $< 7$  Hz) seem to be dominated by the water dynamics signature while higher frequencies ( $> 15$  Hz) may be dominated by the signature of bedload transport. The water activity at low flow or during high water stage may emit quite polarized signals in the horizontal plane. The measured polarization directions of these signals at lower frequencies trend homogeneously toward the closest location of the river stream or points toward a linear segment of the river east of the station. In contrast, signals related to the transport of sediments at higher frequencies are clearly distributed along the whole river segment in the vicinity of the seismic station (from March 5 to 7) inducing a low strength of polarization. Considering this discrimination of physical processes in terms of frequency bands, these findings are consistent with the results from previous observations and from physical models, predicting that the water dynamics has a signature at lower frequency than sediments impacts which have a maximum seismic amplitude between 30 and 40 Hz, and likely above, but out of reach of our sensor recording characteristics. From our observations, we conclude that any study dedicated to the bedload transport quantification should favour small river-to-station distance ( $< 100$  m) for which bedload transport should remain visible over most frequencies. It would be also appropriate to have a collocated rain gauge to constrain the local rainfall signature and to use high sampling rate seismometers to extend the spectra beyond 100 Hz to better analyse the bedload transport signature over a wider frequency band.

This study has demonstrated that despite large uncertainties that still need to be overcome, seismic measurements can bring very interesting information in the survey of large floods in very aggressive environments where direct measurements are not possible. In the future, use of small-scale seismic networks would help understanding the nature of seismic waves and locating noise sources. Finally, well documented sampling of pre and post flood bed grain size distribution and bed topography should help in future studies to better constrain the complex relation that exists between seismic signal and sediment transport.

#### CRedit authorship contribution statement

**A. Gonzalez:** Data curation, Formal analysis, Investigation, Visualization, Writing – original draft. **F.R. Fontaine:** Data curation, Formal analysis, Funding acquisition, Investigation, Methodology, Project administration, Visualization, Writing – original draft, Writing – review & editing. **G. Barruol:** Funding acquisition, Investigation, Methodology, Visualization, Writing – original draft, Writing – review & editing. **A. Recking:** Data curation, Formal analysis, Investigation, Methodology, Validation, Visualization, Writing – original draft, Writing – review & editing. **A. Burtin:** Formal analysis, Visualization, Writing – original draft. **J.-L. Join:** Data curation, Formal analysis, Funding acquisition, Project administration, Validation, Visualization, Writing – original draft, Writing – review & editing. **E. Delcher:** Methodology, Writing – original draft. **L. Michon:** Methodology, Writing – original draft, Writing – review & editing. **F. Gimbert:** Formal analysis, Methodology, Validation, Visualization, Writing – original draft, Writing – review & editing.

#### Declaration of Competing Interest

The authors declare that they have no known competing financial interests or personal relationships that could have appeared to influence the work reported in this paper.

#### Data availability

Seismic data are available at <https://doi.org/10.15778/RESIF.ZF2015>, the remaining data are available at <https://hydro.eaufrance.fr/> and from Météo-France. Ppol package is available upon request.

#### Acknowledgments

This study benefited from support from the Research Federation OMNCG (Observations des Milieux Naturels et des Changements Globaux) and OSU-R (Observatoire des Sciences de l'Univers - de La Réunion) at University of La Réunion, the Région Réunion and the CNRS-INSU (Institut National des Sciences de l'Univers) funding from the TelluS-SYSTEM program. We would like to acknowledge the INSU-RESIF/SISMOB for providing the seismic station deployed in the "Rivière des Pluies" network <https://doi.org/10.15778/RESIF.ZF2015>. Seismic data are available at the French RESIF archive center (<http://seismology.resif.fr>) under the ZF experiment code (Fontaine et al., 2015). This study has been also supported by the ReNovRisk-Erosion FEDER project funded by the Région Réunion and European Community. Thanks to the University of La Réunion and the Laboratoire Géosciences Réunion for their supports. The TISKit package is available at <http://www.ipgp.fr/~crawford/Homepage/Software.html> and the Ppol package upon request to [frfont@ipgp.fr](mailto:frfont@ipgp.fr). We thank Julien Bonnier from Office de l'Eau for his help on the hydrological issues. We also thank Thibault Labadie from Ecole Navale (BCRM Brest) for his contribution on part of the programming.

#### Appendix A. Supplementary data

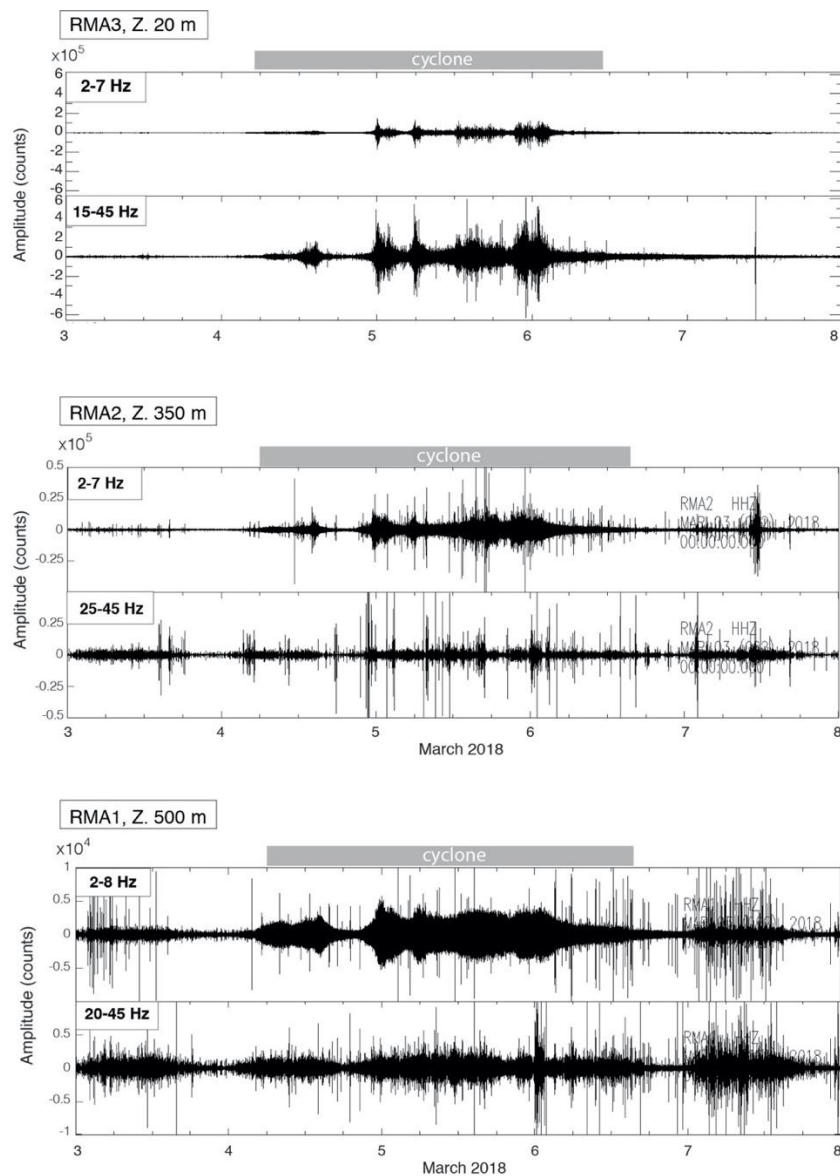
Supplementary data to this article can be found online at <https://doi.org/10.1016/j.jappgeo.2023.105127>.

#### References

- Adams, P.N., Anderson, R.S., Revenaugh, J., 2002. Microseismic measurement of wave-energy delivery to a rocky coast. *Geology* 30, 895–898.
- Arattano, M., 1999. On the use of seismic detectors as monitoring and warning systems for debris flows. *Nat. Hazards* 20 (2–3), 197–213.
- Bakker, M., Gimbert, F., Geay, T., Misset, C., Zanker, S., Recking, A., 2020. Field application and validation of a Seismic Bedload Transport Model. *J. Geophys. Res. Earth Surf.* 125, e2019JF005416 <https://doi.org/10.1029/2019JF005416>.
- Barruol, G., Davy, C., Fontaine, F.R., Schlindwein, V., Sigloch, K., 2016. Monitoring austral and cyclonic swells in the "Iles Eparses" (Mozambique channel) from microseismic noise. *Acta Oecol.* 72 (C), 120–128. <https://doi.org/10.1016/j.actao.2015.10.015>.
- Bathurst, J.C., 2007. Effect of Coarse Surface Layer on Bed-load Transport. *J. Hydraul. Eng.* 133, 1192–1205.
- Battaglia, J., Aki, K., 2003. Location of seismic events and eruptive fissures on the Piton de la Fournaise volcano using seismic amplitudes. *J. Geophys. Res.* 108 <https://doi.org/10.1029/2002JB002193>.
- Boese, C.M., Wotherspoon, L., Alvarez, M., Malin, P., 2015. Analysis of Anthropogenic and Natural Noise from Multilevel Borehole Seismometers in an Urban Environment, Auckland, New Zealand. *Bull. Seismol. Soc. Am.* 105 (1), 285–299. <https://doi.org/10.1785/0120130288>.
- Bokelmann, G.H.R., 1995. P-wave array polarization analysis and effective anisotropy of the brittle crust. *Geophys. J. Int.* 120, 145–162.
- Bret, L., Fevre, Y., Join, J.-L., Robineau, B., Bachelery, P., 2003. Deposits related to degradation processes on Piton des Neiges Volcano (Reunion Island): overview and geological hazard. *J. Volcanol. Geotherm. Res.* 123 (1–2), 25–41. [https://doi.org/10.1016/S0377-0273\(03\)00026-X](https://doi.org/10.1016/S0377-0273(03)00026-X).
- Burtin, A., Bollinger, L., Vergne, J., Cattin, R., Nábělek, J.L., 2008. Spectral analysis of seismic noise induced by rivers: a new tool to monitor spatiotemporal changes in stream hydrodynamics. *J. Geophys. Res.* 113 (B5), 911. <https://doi.org/10.1029/2007JB005034>.
- Burtin, A., Cattin, R., Bollinger, L., Vergne, J., Steer, P., Robert, A., Findling, N., Tiberi, C., 2011. Towards the hydrologic and bed load monitoring from high-frequency seismic noise in a braided river: The "torrent de St Pierre," French Alps. *J. Hydrol.* 408 (1–2), 43–53. <https://doi.org/10.1016/j.jhydrol.2011.07.014>.
- Chao, W.-A., Wu, Y.-M., Zhao, L., Tsai, V.C., Chen, C.-H., 2015. Seismologically determined bedload flux during the typhoon season. *Sci. Rep.* 5 (1) <https://doi.org/10.1038/srep08261>, 13,971–8.
- Church, M., Hassan, M.A., Wolcott, J.F., 1998. Stabilizing self-organized structures in gravel-bed stream channels: Field and experimental observations. *Water Resour. Res.* 34 (11), 3169–3179.

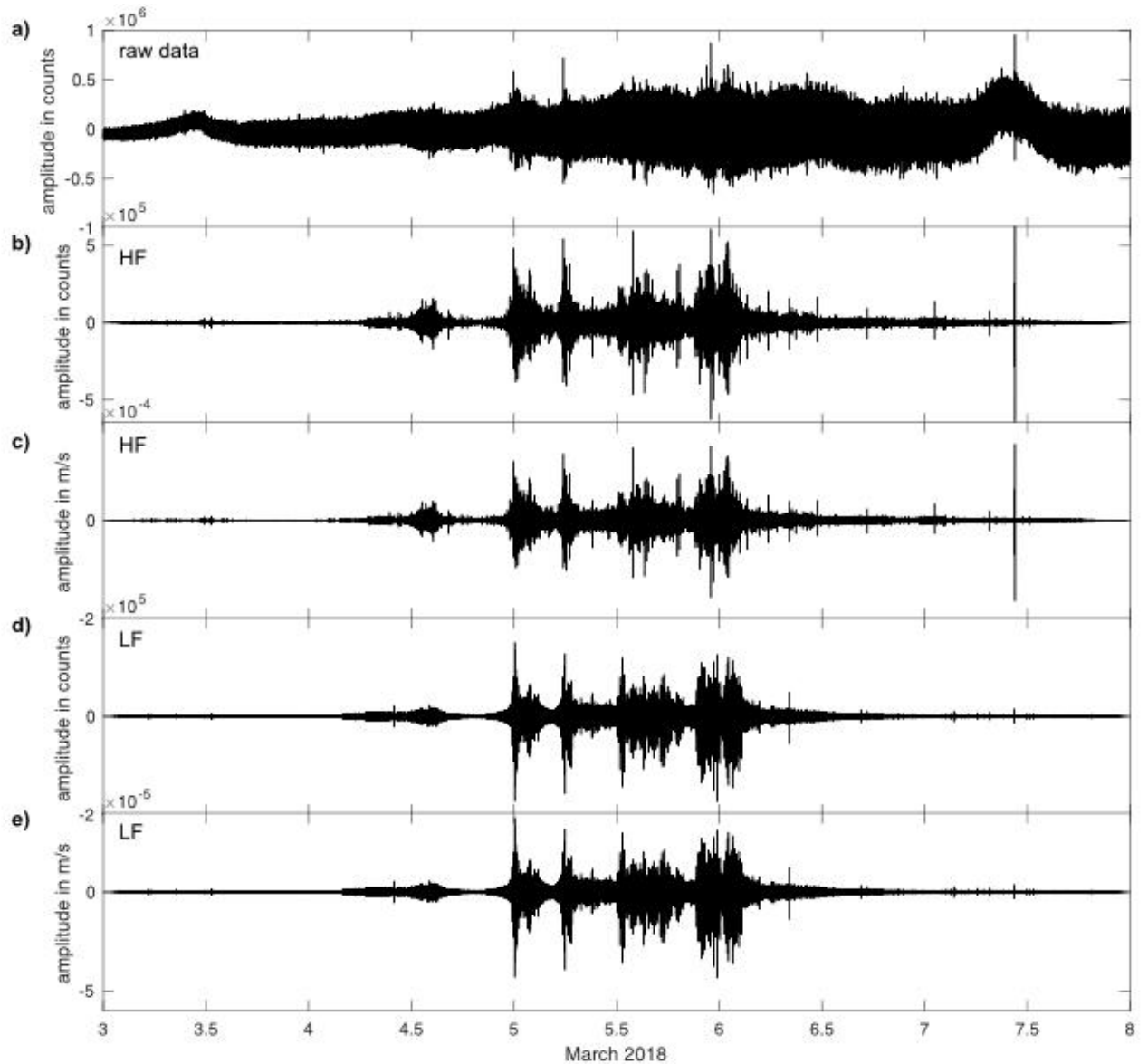
- Davy, C., Barruol, G., Fontaine, F.R., Sigloch, K., Stutzmann, E., 2014. Tracking major storms from microseismic and hydroacoustic observations on the seafloor. *Geophys. Res. Lett.* 41 (24), 8825–8831. <https://doi.org/10.1002/2014GL062319>.
- Davy, C., Barruol, G., Fontaine, F.R., Cordier, E., 2016. Analyses of extreme swell events on La Réunion Island from microseismic noise. *Geophys. J. Int.* 207 (3), 1767–1782. <https://doi.org/10.1093/gji/ggw365>.
- De la Torre, Y., 2008. Etude hydrogéomorphologique de la Rivière du Mât et propositions de solutions de gestion. BRGM Report, RP-56364-FR, pp. 1–356.
- Dean, T., 2017. The seismic signature of rain. *Geophysics* 82, 53–60.
- Deparis, J., Jongmans, D., Cotton, F., Baillel, L., Thouvenot, F., Hantz, D., 2008. Analysis of Rock-fall and Rock-fall Avalanche Seismograms in the French Alps. *Bull. Seismol. Soc. Am.* 98 (4), 1781–1796. <https://doi.org/10.1785/0120070082>.
- Eibl, E.P.S., Lokmer, I., Bean, C.J., Akerlie, E., Vogfjörð, K.S., 2015. Helicopter vs. volcanic tremor: characteristic features of seismic harmonic tremor on volcanoes. *J. Volcanol. Geotherm. Res.* 304 (C), 108–117. <https://doi.org/10.1016/j.jvolgeores.2015.08.002>.
- Fernandez Luque, R., van Beek, R., 1976. Erosion and transport of bed-load sediment. *J. Hydraul. Res.* 14 (2), 127–144. <https://doi.org/10.1080/00221687609499677>.
- Flinn, E.P., 1965. Signal analysis using rectilinearity and direction particle motion. *Proc. IEEE* 12, 1874–1876.
- Fontaine, F.R., Barruol, G., Kennet, B.L.N., Bokelmann, G.H.R., Reymond, D., 2009. Upper mantle anisotropy beneath Australia and Tahiti from Pwave polarization: Implications for real-time earthquake location. *J. Geophys. Res.* 114 (B3) <https://doi.org/10.1029/2008JB005709>.
- Fontaine, F.R., Barruol, G., Gonzalez, A., 2015. Rivière des Pluies Project, La Réunion Island, 2015–2018. RESIF - Réseau Sismologique et géodésique Français. <https://doi.org/10.15778/RESIF.ZF2015>.
- Gayer, E., Michon, L., Louvat, P., Gaillardet, J., 2019. Storm-induced precipitation variability control of long-term erosion. *Earth Planet. Sci. Lett.* 517, 61–70. <https://doi.org/10.1016/j.epsl.2019.04.003>.
- Gimbert, F., Tsai, V.C., Lamb, M.P., 2014. A physical model for seismic noise generation by turbulent flow in rivers. *J. Geophys. Res. Earth Surf.* 119 (10), 2209–2238. <https://doi.org/10.1002/2014JF003201>.
- Gonzalez, A., 2019. Suivi sismologique de l'impact des cyclones sur la charge de fond de la Rivière des Pluies et de la Rivière du Mât à La Réunion. Doctorat Thesis, Université de La Réunion, La Réunion, 146pp.
- Goodling, P.J., Lekic, V., Prestegard, K., 2018. Seismic signature of turbulence during the 2017 Oroville Dam spillway erosion crisis. *Earth Surf. Dyn.* 351–367. <https://doi.org/10.5194/esurf-6-351-2018>.
- Govi, M., Maraga, F., Moia, F., 1993. Seismic detectors for continuous bed load monitoring in a gravel stream. *Hydrol. Sci. J.* 38 (2), 123–132. <https://doi.org/10.1002/esp.3290100107>.
- Herrmann, R.B., 2013. Computer Programs in Seismology: An Evolving Tool for Instruction and Research. *Seismol. Res. Lett.* 84 (6), 1081–1088. <https://doi.org/10.1785/0220110096>.
- Hsu, L., Finnegan, N.J., Brodsky, E.E., 2011. A seismic signature of river bedload transport during storm events. *Geophys. Res. Lett.* 38 (13) <https://doi.org/10.1029/2011GL047759>.
- Jurkevics, A., 1988. Polarization analysis of three-component array data. *Bull. Seismol. Soc. Am.* 78, 1725–1743.
- Kramer, R., Lu, Y., Bokelmann, G., 2023. Interaction of Air pressure and Groundwater as Main Cause of Sub-Daily Relative Seismic Velocity changes. *Geophys. Res. Lett.* 50 (7), e2022GL101298.
- Kuzma, H.A., Fernandez-Martinez, J.-L., Zhao, Y., Dunson, C., Zhai, M.-Y., Mangriotis, M.-D., Rector, J.W., 2008. Vehicle traffic as a source for near-surface passive seismic imaging. *Environ. Eng. Geophys. Soc.* 1–8.
- Lenzi, M.A., Mao, L., Comiti, F., 2006. When does bedload transport begin in steep boulder-bed streams? *Hydrol. Process.* 20, 3517–3533.
- MacKenzie, L.G., Eaton, B.C., Church, M., 2018. Breaking from the average: why large grains matter in gravel-bed streams. *Earth Surf. Process. Landf.* 43 (15), 3190–3196. <https://doi.org/10.1002/esp.4465>.
- Mao, S., Campillo, M., van Der Hilst, R.D., Brenguier, F., Stehly, L., Hillers, G., 2019. High temporal resolution monitoring of small variations in crustal strain by dense seismic arrays. *Geophys. Res. Lett.* 46 (1), 128–137.
- McNutt, S.R., 1992. Volcanic tremor. *Encycl. Earth Syst. Sci.* 4, 417–425.
- Nanni, U., Gimbert, F., Vincent, C., Gräff, D., Walter, F., Piard, L., Moreau, L., 2020. Quantification of seasonal and diurnal dynamics of subglacial channels using seismic observations on an Alpine glacier. *Cryosphere* 14 (5), 1475–1496. <https://doi.org/10.5194/tc-14-1475-2020>.
- Peterson, J., 1993. Observations and modeling of seismic background noise. U.S. Department of interior geological survey, pp. 1–94.
- Piantini, M., Gimbert, F., Bellot, H., Recking, A., 2021. Genesis and propagation of exogenous sediment pulses in mountain channels: insights from flume experiments with seismic monitoring. *Earth Surf. Dyn.* <https://doi.org/10.5194/esurf-2021-28>.
- Réchou, A., Flores, O., Jumaux, G., Duflot, V., Bousquet, O., Pouppeville, C., Bonnardot, F., 2019. Spatio-temporal variability of rainfall in a high tropical island: patterns and large-scale drivers in Réunion Island. *Q.J.R. Meteorol. Soc.* 145 (720), 893–909. <https://doi.org/10.1002/qj.3485>.
- Recking, A., 2009. Theoretical development on the effects of changing flow hydraulics on incipient bedload motion. *Water Resour. Res.* 45, W04401. <https://doi.org/10.1029/2008WR006826>.
- Recking, A., Frey, P., Paquier, A., Belleudy, P., 2009. An experimental investigation of mechanisms involved in bed load sheet production and migration. *J. Geophys. Res.* 114 (F3) <https://doi.org/10.1029/2008JF000990>, 1176–13.
- Recking, A., 2010. A comparison between flume and field bed load transport data and consequences for surface-based bed load transport prediction. *Water Resour. Res.* 46 (3), 896–916. <https://doi.org/10.1029/2009WR008007>.
- Recking, A., 2012. Influence of sediment supply on mountain streams bedload transport rates. *Geomorphology* 175–176, 139–150.
- Recking, A., Piton, G., Vazquez-Tarrio, D., Parker, G., 2016. Quantifying the morphological print of bedload transport. *Earth Surf. Process. Landf.* 41, 809–822. <https://doi.org/10.1002/esp.3869>.
- Reymond, D., 2010. Différentes approches pour une estimation rapide des paramètres de source sismique : application pour l'alerte aux tsunamis. Doctorat Thesis, Université de Polynésie française, Tahiti, 300pp.
- Rindharisaona, E.J., Réchou, A., Fontaine, F.R., Barruol, G., Stamenoff, P., Boudevillain, B., Rigaud-Louise, F., Delcher, E., 2022. Seismic signature of rain and wind inferred from seismic data. *Earth Space Sci.* 9 (10), e2022EA002328 <https://doi.org/10.1029/2022EA002328>.
- Roth, D.L., Brodsky, E.E., Finnegan, N.J., Rickenmann, D., Turowski, J.M., Badoux, A., 2016. Bed load sediment transport inferred from seismic signals near a river. *J. Geophys. Res. Earth Surf.* 121 (4), 725–747. <https://doi.org/10.1002/2015JF003782>.
- Roth, D.L., Finnegan, N.J., Brodsky, E.E., Rickenmann, D., Turowski, J.M., Badoux, A., Gimbert, F., 2017. Bed load transport and boundary roughness changes as competing causes of hysteresis in the relationship between river discharge and seismic amplitude recorded near a steep mountain stream. *J. Geophys. Res. Earth Surf.* 122 (5), 1182–1200. <https://doi.org/10.1002/2016JF004062>.
- Schmandt, B., Aster, R.C., Scherler, D., Tsai, V.C., Karlstrom, K., 2013. Multiple fluvial processes detected by riverside seismic and infrasound monitoring of a controlled flood in the Grand Canyon. *Geophys. Res. Lett.* 40 (18), 4858–4863. <https://doi.org/10.1002/grl.50953>.
- Scholz, J.-R., Barruol, G., Fontaine, F.R., Sigloch, K., Crawford, W.C., Deen, M., 2017. Orienting Ocean-bottom seismometers from P-wave and Rayleigh wave polarizations. *Geophys. J. Int.* 208, 1277–1289.
- Schöpa, A., Chao, W.-A., Lipovsky, B., Hovius, N., White, R.S., Green, R.G., Turowski, J.M., 2017. Dynamics of the Askja caldera July 2014 landslide, Iceland, from seismic signal analysis: precursor, motion and aftermath. *Earth Surf. Dyn. Discuss* 1–34. <https://doi.org/10.5194/esurf-2017-68>.
- Stachnik, J.C., Sheehan, A.F., Zietlow, D.W., Yang, Z., Collins, J., Ferris, A., 2012. Determination of New Zealand Ocean Bottom Seismometer Orientation via Rayleigh-Wave Polarization. *Seismol. Res. Lett.* 83, 704–713.
- Tsai, V.C., Minchew, B., Lamb, M.P., Ampuero, J.-P., 2012. A physical model for seismic noise generation from sediment transport in rivers. *Geophys. Res. Lett.* 39 (2) <https://doi.org/10.1029/2011GL050255>.
- Turowski, J.M., Yager, E.M., Badoux, A., Rickenmann, D., Molnar, P., 2009. The impact of exceptional events on erosion, bedload transport and channel stability in a step-pool channel. *Earth Surf. Process. Landf.* 34 (12), 1661–1673. <https://doi.org/10.1002/esp.1855>.
- Wessel, P., Smith, J.B., 1991. Free software helps map and display data. *Eos Trans. AGU* 1–5.
- Wilcock, P., 1997. Entrainment, displacement and transport of tracer gravels. *Earth Surf. Process. Landf.* 22, 1125–1138.
- Wilcock, P.R., McArdell, B.W., 1993. Surface-based Fractional Transport rates : Mobilization Thresholds and Partial Transport of a Sand-Gravel Sediment. *Water Resour. Res.* 29, 1297–1312.
- Wolman, M.G., 1954. A method of sampling coarse river-bed material. *Eos Trans. AGU* 35, 1–6.

## Supplementary material



### Appendix A1: Seismic waveform for both LF and HF recorded at the three studied stations.

Seismic waveforms recorded respectively at stations (top) RMA3, (middle) RMA2 and (bottom) RMA1 during the cyclone Dumazile (March 3 to 8, 2018) band-pass filtered in the low and high frequency bands (indicated on each plot), showing the smaller amplitude at low frequency than at high frequencies. Note the vertical scale is fixed for each station but different between the three stations.

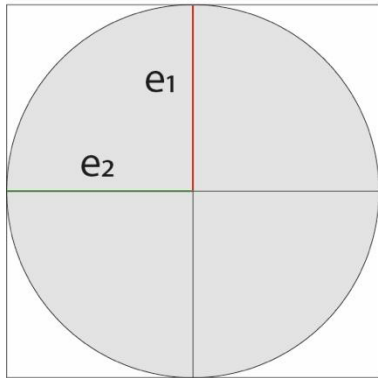


### Appendix A2: Instrument response correction

a) Raw seismic signal recorded at RMA3 station on the vertical component. Before filtering, we removed the mean signal, removed the trend and applied a 5% Hanning taper. The signal from the vertical component of RMA3 station was bandpass filtered with a zero-phase 4-pole Butterworth filter between 15-45 Hz (HF). Filtered seismic waveform before (b) and after (c) applying the instrument response: the filtered data of each station was multiplied by the sensor sensitivity of each of them as the corresponding instrumental responses of the seismometers are flat in the frequency considered in this study. Filtered signal from the vertical component of RMA3 station between 2-7 Hz (LF) before (d) and after (e) applying the instrument response.

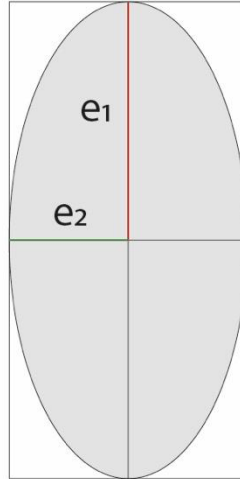
**$C_{pH/Z} = 0$**

*circular  
mouvement*



**$C_{pH/Z} = 0,5$**

*ellipsoidal  
mouvement*



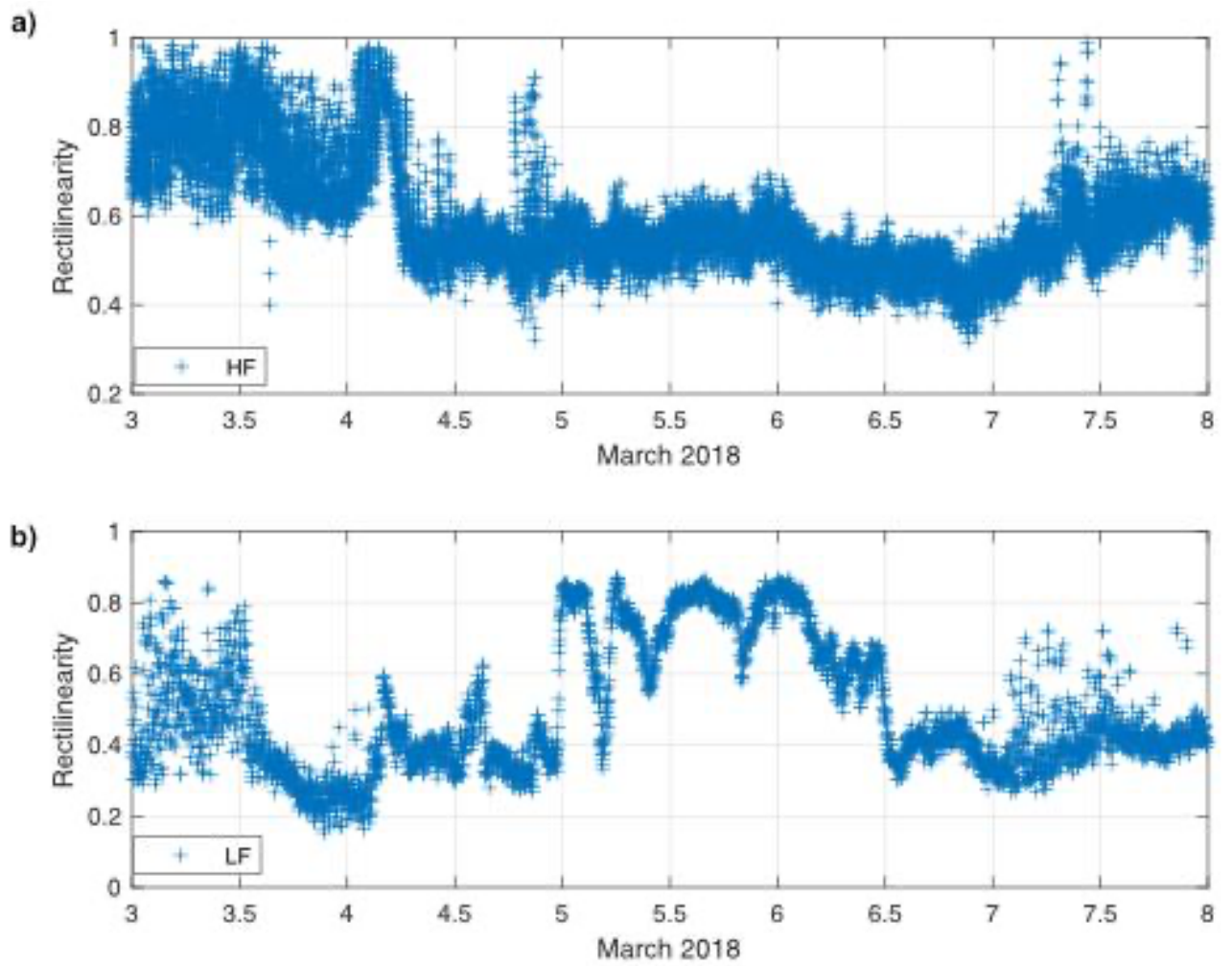
**$C_{pH/Z} = 1$**

*linear mouvement*



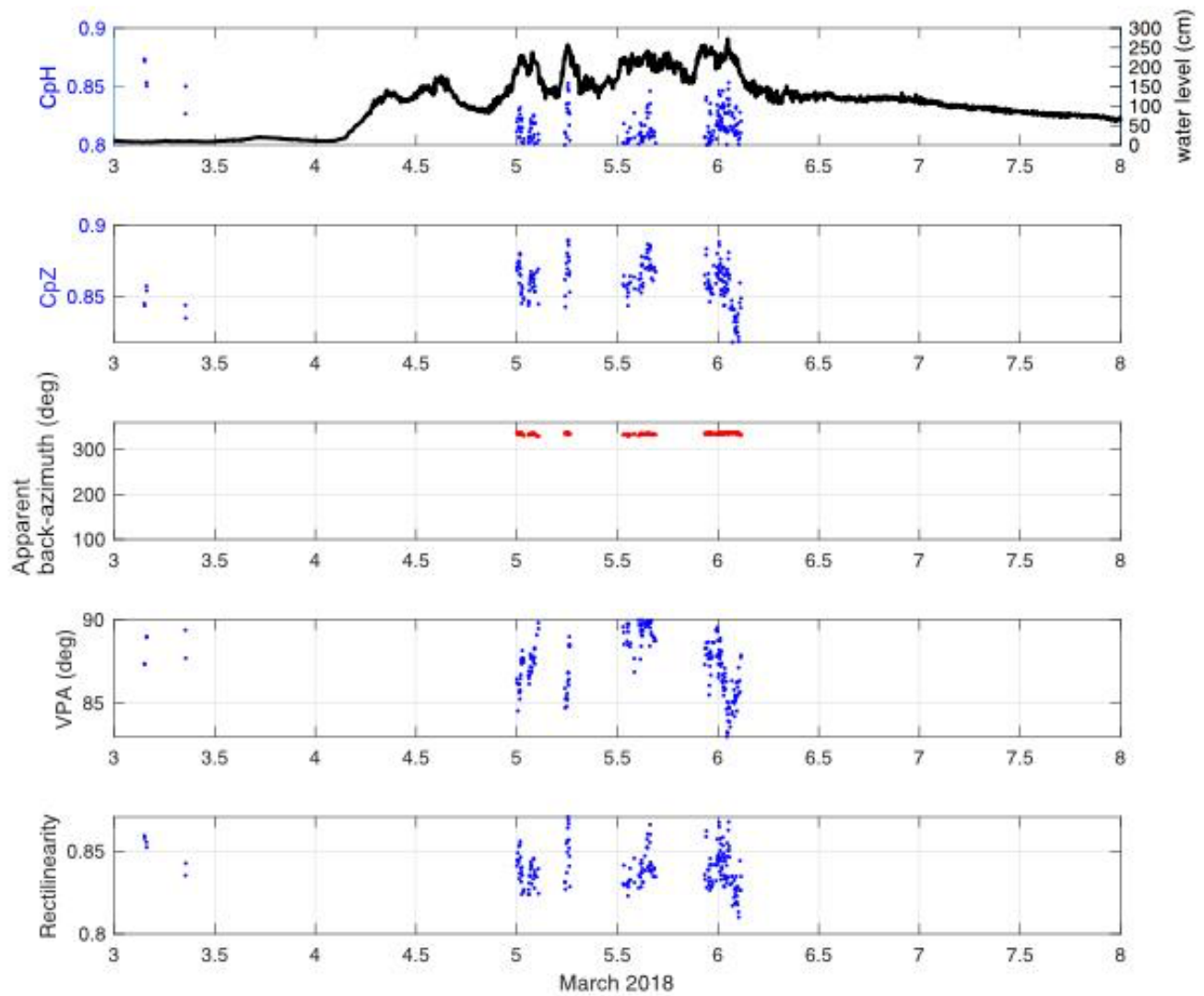
### **Appendix B: Rectilinearity coefficient in the horizontal and vertical plane**

Sketch of the shape of the ground particles movement depending on the rectilinearity coefficient in the horizontal plane  $C_{pH}$  or vertical plane  $C_{pZ}$ .  $C_{pH}$  and  $C_{pZ}$  are equal to 0 for a circular polarization, 0.5 for an ellipsoidal polarization and to 1 for a purely linear polarization ( $e_2$  and  $e_1$  are the eigenvalues of the covariance matrix obtained from the two horizontal components with  $e_2 \leq e_1$ ).



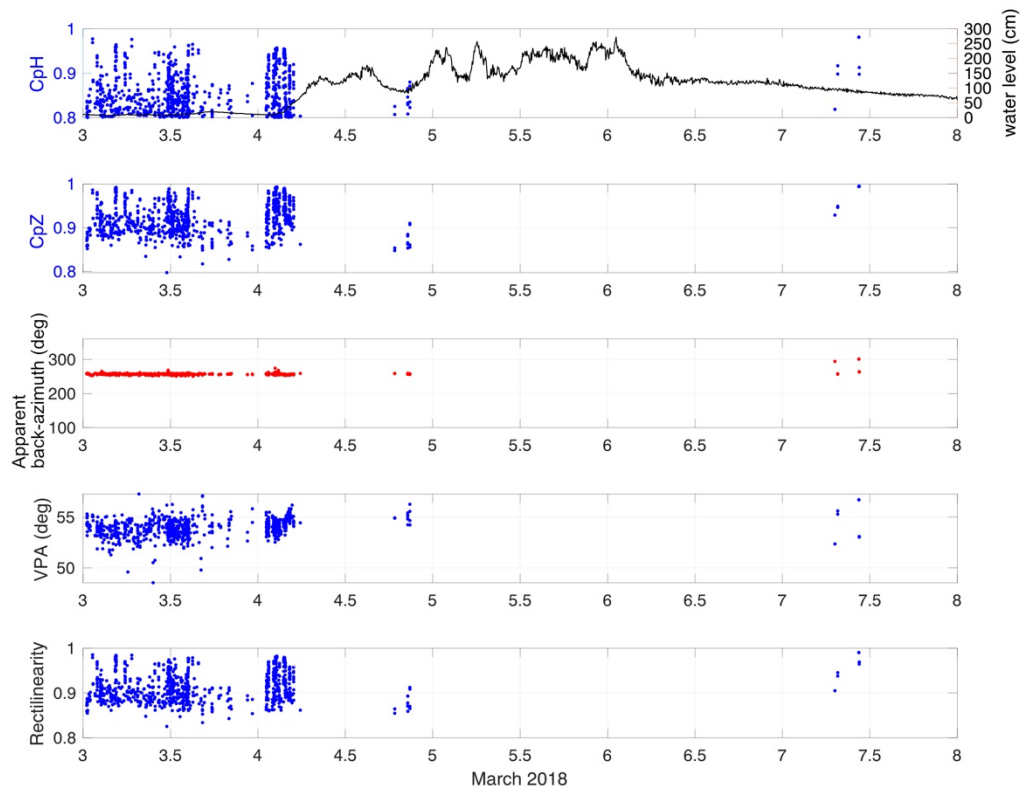
### Appendix C: Rectilinearity of particle motion at seismic station RMA3

Variation of the rectilinearity of particle motion at seismic station RMA3 in the HF (a) and LF (b) band showing the very different behaviour in the two bands.



**Appendix D1: Polarization measurements compared to the water level variation, performed at RMA3 in the LF (low frequency) band.**

These measurements evidence the quasi-linear ground motions observed in the LF band at RMA3 station. On these graphs, only measurements for  $CpH$  values  $> 0.8$  are represented in order to identify quasi-linear ground motions. Note that they clearly occur during peaks of the water level.



**Appendix D2: Polarization measurements compared to the water level variation at station RMA3 in the HF (high frequency) band and for  $CpH$  values  $> 0.8$ .**

Note the absence of significant polarization during the flood in the HF band.